

Cancelled as
_{NBS} IR-80-1998

Report Number AFOSR-TR-80-0476

Defense Technical Information
Center Accession No. ADA-086283

IGNITION OF A LIQUID FUEL UNDER HIGH INTENSITY RADIATION

Final Progress Report including progress from
May 1, 1978 to September 30, 1979

Takashi Kashiwagi
Howard R. Baum
and
John A. Rockett

Center for Fire Research
National Bureau of Standards
Washington, D.C. 20234

This work is supported by the Air Force Office of Scientific Research
under Contract AFOSR-ISSA-79-0006

Approved for public release; distribution unlimited

Qualified requestors may obtain additional copies from the Defense Technical Information Center, all others should apply to the National Technical Information Service.

Conditions of Reproduction

Reproduction, translation, publication, use and disposal in whole or in part by or for the United States Government is permitted.

UNCLASSIFIED

SECURITY CLASSIFICATION OF THIS PAGE (When Data Entered)

REPORT DOCUMENTATION PAGE		READ INSTRUCTIONS BEFORE COMPLETING FORM
1. REPORT NUMBER AFOSR-TR-80-0476	2. GOVT ACCESSION NO. ADA-086283	3. RECIPIENT'S CATALOG NUMBER
4. TITLE (and Subtitle) IGNITION OF A LIQUID FUEL UNDER HIGH INTENSITY RADIATION		5. TYPE OF REPORT & PERIOD COVERED FINAL 1 May 78 - 20 Sep 79
7. AUTHOR(s) TAKASHI KASHIWAGI HOWARD R BAUM JOHN A ROCKETT		6. PERFORMING ORG. REPORT NUMBER AFOSR-ISSA-79-0006
9. PERFORMING ORGANIZATION NAME AND ADDRESS CENTER FOR FIRE RESEARCH NATIONAL BUREAU OF STANDARDS WASHINGTON, DC 20234		10. PROGRAM ELEMENT, PROJECT, TASK AREA & WORK UNIT NUMBERS 2308A2 61102F
11. CONTROLLING OFFICE NAME AND ADDRESS AIR FORCE OFFICE OF SCIENTIFIC RESEARCH/NA BUILDING 410 WASHINGTON, DC 20332		12. REPORT DATE January 1980
14. MONITORING AGENCY NAME & ADDRESS(if different from Controlling Office)		13. NUMBER OF PAGES 65
		15. SECURITY CLASS. (of this report) UNCLASSIFIED
		15a. DECLASSIFICATION/DOWNGRADING SCHEDULE
16. DISTRIBUTION STATEMENT (of this Report) Approved for public release; distribution unlimited.		
17. DISTRIBUTION STATEMENT (of the abstract entered in Block 20, if different from Report)		
18. SUPPLEMENTARY NOTES		
19. KEY WORDS (Continue on reverse side if necessary and identify by block number) RADIATIVE IGNITION MECHANISMS LASER SUPPORTED IGNITION AND COMBUSTION HYDROCARBON IGNITION AIRCRAFT FUEL IGNITION AIRCRAFT FIRES AND EXPLOSIONS		
20. ABSTRACT (Continue on reverse side if necessary and identify by block number) This report summarizes progress in the study of ignition of a liquid fuel under high intensity radiation. It describes an experimental study of the key processes during ignition and a theoretical modeling study of part of the phenomena during the ignition period. The experiments were conducted using a CW CO ₂ laser with incident fluxes from 1000 to 5000 W/cm ² and n-decane as the flammable liquid. High speed photographs of ignition events showed a periodic depression in the decane surface, probably caused by the thrust of the strong decane vapor flux; radial outward motion of the liquid, probably caused by a surface		

~~UNCLASSIFIED~~

~~SECURITY CLASSIFICATION OF THIS PAGE(When Data Entered)~~

tension, gradient was also observed. The first appearance of flame was in the gas phase well above the surface. The proposed autoignition mechanism of decane by the CO₂ laser is the absorption of the incident laser beam by the vapor plume. The effect on ignition of the incident angle of the laser beam with respect to the decane surface was studied from 90° to 30°. On reducing the incident angle, the ignition delay time becomes longer and the minimum incident flux for ignition increases significantly. A theoretical model describing the flow motion in the gas phase caused by a heated surface was calculated numerically and solved analytically.

~~UNCLASSIFIED~~

~~SECURITY CLASSIFICATION OF THIS PAGE(When Data Entered)~~

IGNITION OF A LIQUID FUEL UNDER HIGH INTENSITY RADIATION

Takashi Kashiwagi, Howard R. Baum and John A. Rockett

Abstract

This report summarizes progress in the study of ignition of a liquid fuel under high intensity radiation; the period covered is from May 1, 1977 to September 30, 1979. It describes an experimental study of the key processes during ignition and a theoretical modeling study of part of the phenomena during the ignition period. The experiments were conducted using a CW CO₂ laser with incident fluxes from 1000 to 5000 W/cm² and n-decane as the flammable liquid. High speed photographs of ignition events showed a periodic depression in the decane surface, probably caused by the thrust of the strong decane vapor flux; radial outward motion of the liquid, probably caused by a surface tension gradient was also observed. The first appearance of flame was in the gas phase well above the surface. The proposed autoignition mechanism of decane by the CO₂ laser is the absorption of the incident laser beam by the vapor plume. The effect on ignition of the incident angle of the laser beam with respect to the decane surface was studied from 90° to 30°. On reducing the incident angle, the ignition delay time becomes longer and the minimum incident flux for ignition increases significantly. A theoretical model describing the flow motion in the gas phase caused by a heated surface was calculated numerically and solved analytically.

1. INTRODUCTION

Laser technology has been rapidly advancing in the last several years. Power outputs of modern lasers have increased significantly and these lasers can now be used as tactical weapons. A high power laser weapon can ignite aircraft fuel by fuel tank penetration and can thus cause a fire or explosion on the aircraft. However, the ignition of flammable liquids by laser radiation has been little studied and is little understood; the ignition of solids [1,2] and the vaporization of liquids by high power lasers [3,4] have been studied. The objective of this study is to obtain a fundamental understanding of the mechanism of ignition of flammable liquids by a high power laser.

This paper is a final progress report of this study during the period from May 1977 to September 1979. It describes an experimental study of the key processes during ignition and a theoretical study of the modeling of a part of the phenomena during the ignition period.

2. EXPERIMENTAL APPARATUS

A schematic illustration of the experimental apparatus is provided in figure 1. A photograph of the equipment is shown in figure 2. A Coherent Radiation Model 41 CO₂ laser* emits an approximately 5 mm diameter beam at 1/e intensity. Beam power can be varied from 240 to 350 watts in the fundamental mode with a Gaussian power distribution across the beam. The incident flux distribution at the sample surface position is measured at normal incidence prior to each ignition experiment by traversing a water cooled calorimeter with 0.25 mm diameter sensing

*In order to adequately describe materials and experimental procedures it was occasionally necessary to identify commercial products by manufacturer's name or label. In no instance does such identification imply endorsement by the National Bureau of Standards nor does it imply that the particular product or equipment is necessarily the best available for that purpose.

element. The maximum value of the incident flux measured in this manner is used as the incident radiant flux in this study.

A rotating mirror is used as a shutter to provide a step-function irradiance and remains open through the ignition event. Ignition is defined by the first light emission detected by an EMI 7656 photomultiplier, the output of which is recorded by an oscillographic recorder with maximum resolution of ± 1 msec. At the onset of flaming, a step-function-like output of the photomultiplier is observed. This provides an unambiguous measure of the time of ignition. In this study, n-decane was used as the liquid fuel and air as the environmental gas.

The experimental chamber is 34 cm inside diameter with 40 cm depth. The chamber is mounted on bearings and can be rotated 90 degrees by a worm gear. The incident angle of the laser beam is varied by changing locations of two mirrors and by the rotation of the chamber as shown in figure 1. After each ignition test, the gas in the chamber is evacuated by a vacuum pump and fresh air admitted.

The fuel container is fastened onto a support plate which is mounted on the chamber wall. When the chamber rotates, the support plate tilts and the axis of the container is along the incident laser beam. To make the container top parallel to the horizontal decane surface, the top of the container is cut to be horizontal when it is tilted, thus a separate container is needed for each angle. Decane is always filled to the top of the container.

A square aluminum container with schlieren quality glass windows for two sides was used when high speed motion pictures were taken to observe the flow motion in decane near the decane surface.

3. EXPERIMENTAL RESULTS

The first series of experiments was conducted to find a container size which did not affect ignition delay time under various experimental conditions. The effect of the depth of the container on ignition delay time was studied with a 5 cm diameter container under the vertical radiation mode (incident angle $\theta = 90^\circ$). The depth of the container was varied from 1.2 cm to 34 cm. Ignition delay times with various depths are shown in figure 3, which indicate little effect of depth on ignition delay time.

Similarly, the effect of the diameter of the container on ignition delay time was studied with a 5 cm deep container at $\theta = 90^\circ$ under two different incident radiant fluxes. The diameter of the container was varied from 2.5 cm to 10 cm. Results are shown in figure 4a at the incident radiant flux $I_o = 4160 \text{ W/cm}^2$ and in figure 4b at $I_o = 1670 \text{ W/cm}^2$. At high flux, there was no effect of the diameter of the container on ignition delay time. But at low flux, ignition delay time became significantly longer for the container whose diameter was less than 4 cm. Apparently the motion in the liquid, which will be described later, causes some heat loss to the container wall and delays the ignition. From these results, a container of 6 cm diameter and 5 cm depth filled to the top was selected and used for all experiments described in this report.

In ignition experiments, bursting sounds similar to those when water droplets fall onto a heated plate were clearly heard during the ignition period, indicating the rapid boiling of decane during the experiment. At low

radiant flux a large volume of decane was heated during the long ignition delay and a large amount of decane evaporated. Under these conditions, ignition was associated with a puff sound and the size of the flame immediately after ignition tended to be larger than that at high incident radiant flux.

Two types of high speed motion pictures were taken to observe the behavior of the decane surface and the onset of ignition; some were taken from the top and others were taken from the side through the glass window. Some enlarged frames of the former are shown in figure 5. The incident angle of the laser beam to the surface was 30 degrees and the shape of the container top was the cross sectional cut of a cylinder tilted at 60 degrees. The direction of the laser beam was from the left. The top figure (5a) shows decane surface in the container before the laser irradiates the decane. The figure (5b) shows the development of surface waves traveling rapidly outward from the irradiated area shortly after the laser irradiation was started. Surface waves traveled rapidly along the surface, shown in figure (5c), and reached the wall of the container as shown in figure 5d. Under the low incident flux used in figure 5, surface waves could reach the wall and be reflected. Under the high incident flux, ignition occurred before the surface waves reached the wall. In figure 5e, the onset of ignition was observed in the gas phase far from the decane surface, (light area at the left above the surface). Rapid flame spread along the plume of the decane vapor was observed immediately after ignition as shown in figure 5f. High speed color pictures, under the high incident flux, show a small, bright yellow rod shape of color at the location where the incident laser beam interacted with the plume of the decane vapor. This was a much brighter color than the rest of the flame and it remained until the laser beam was turned off.

The side view of the behavior of the decane surface is shown in figures 6 and 7. In figure 6, the incident angle of the laser beam from the left to the surface, θ , was 30 degrees. In figure 7, the incident angle was 90 degrees and the pictures are negative. Both figures show that a bubble like depression at the surface is formed shortly after the irradiation starts and this depression grows rapidly to about 3 mm diameter. We infer that the depression is due to vaporization thrust and is not a bubble since: (1) if it were a bubble, then its top surface would be irradiated in the area of peak flux and would be vaporized immediately upon formation leaving the bubble open to collapse and, (2) the early pictures indicate vaguely a rising plume of decane vapor above the depression. This implies vigorous vaporization instead of bubble formation (which implies weak vaporization).

In figures 6 and 7, about 10 msec after the irradiation starts, the depression has started to collapse. At $\theta = 30^\circ$, the depression started to collapse from the left side from which the incident laser beam was coming. However, at $\theta = 90^\circ$, the depression collapsed symmetrically to small bubbles. At $\theta = 30^\circ$, the formation of the next depression took about 40 msec, but at $\theta = 90^\circ$, the next depression was formed rapidly after a delay of about 10 to 15 msec. At $\theta = 30^\circ$, the second depression was smaller and not as distinct as the first one and the depression tended to be formed more distinctly at the side opposite that of the approaching incident laser beam. Again, the second depression collapsed and this cycle of the formation of the depression and its collapse was repeated during the ignition period and even after ignition. At $\theta = 90^\circ$, this cycle was repeated with much faster frequency than that at $\theta = 30^\circ$. At $\theta = 30^\circ$, the first appearance of flame was about 10 mm above the decane surface and about 20 mm away from the irradiated area. Flame spread from the point of first appearance of flame upward, presumably due to buoyancy, and then spread toward the irradiated area of the decane surface along the laser beam. The

observed rod shape flame is similar to that shown in figure 5. At $\theta = 90^\circ$, the first appearance of flame was above the viewing area of the picture and the flame spread down, as is shown in figure 7.

It is interesting to analyze the mechanism of the formation of the depression more closely. Since the depression distance caused by photon pressure with the flux range used in this study is at most 0.1 mm compared to the observed 3 mm, the effect of photon pressure on the formation of the depression is negligible. Vigorous vaporization of decane by the incident flux used in this study can produce a significant momentum flux leaving the surface which in turn presses down on that surface. The momentum of the decane vapor leaving the surface should be balanced with the surface tension force caused by the area increase and the hydrostatic force. The velocity of decane vapor leaving the surface can be estimated from this balance.

$$\frac{2r}{R} + \rho gh = \rho_g v_g^2 \quad (1)$$

where r is the surface tension, 23.4 g/sec² for decane [5], R is the radius of the depression, 3 mm, ρ liquid decane density, 0.73 g/cm³, h distance of the surface depression, 3 mm, and ρ_g density of decane vapor at boiling temperature 174°C [6], 0.00423 g/cm³. Then, the velocity of decane vapor leaving the surface v_g is approximately

$$v_g \approx 300 \text{ cm/sec}$$

From close examination of the pictures in figures 6 and 7, the speed of the rising plume is at least this order of magnitude. The amount of the energy required to produce this rate of vaporization of decane is estimated by

$$\rho_g v_g Q$$

where Q is latent of heat of vaporization of decane, 263 J/g [5]. Then, using the same values for ρ_g and V_g as above, the endothermic flux for vaporization is about 330 W/cm^2 which is well below the incident radiant flux. Therefore, the incident radiant flux in this study is high enough to provide the estimated amount of vaporization needed to cause the observed depression on the decane surface. Therefore, it is reasonable to consider that the surface depression observed during the ignition period is in fact caused by the momentum of decane vapor leaving the decane surface. A further confirmation that the vigorous vaporization causes the depression of the decane surface by its momentum was attempted by taking high speed schlieren pictures during the ignition period. Preliminary study of these indicates that the vaporization of decane in the present experimental condition behaves like an explosion and it appears to throw off not only decane vapor but also fragments of liquid decane, as shown in figure 8. However, further study with more high speed schlieren pictures is necessary to confirm this mechanism.

The boiling temperature of decane is 174°C [6] and the gas phase temperature near the surface could rise to this temperature by conduction/convection from the decane surface. However, this is too low a temperature to initiate a gas phase chemical reaction and to attain a runaway condition (roughly 600°C is required for ignition [7]). From the observation of the location of the first appearance of flame in figures 5 and 6, it is apparent that the absorption of the laser beam by the decane vapor is the key heating mechanism in the gas phase causing ignition. This was confirmed by the ignition of vapor from decane heated on an electrical hot plate by passing the laser beam through the vapor parallel to but above the liquid decane surface.

To absorb enough energy from the laser beam to heat the gas phase to ignition, a sufficient amount of decane vapor is required at the location of the first appearance of flame. Judging from the distance between the irradiated area and the ignition location shown in figure 6, the transport process of decane vapor from the surface to the location of the first appearance of flame may well be the key factor for ignition under low incident laser angles. As described above, decane vapor/decane fragments are released from the decane surface with significant inertia into the gas phase. It appears in figure 8 that this explosion like vaporization could distribute a sufficient amount of momentum for decane vapor/fragments to go in all directions. However, in figure 6, the release of decane vapor appears directly upward rather than in all directions (although the pictures are direct rather than schlieren). Since the density of decane vapor at its boiling temperature is much greater than that of air, decane vapor will tend to sink back to the decane surface. After decane vapor is released into the gas phase by the jet-like flow, cooled decane vapor starts to fall and may intersect the laser beam. The direction of the release of decane vapor/fragments is presently not conclusive. Further study is necessary to clarify the transport process of decane vapor/fragments from the irradiation surface to the location of the first appearance of flame.

The periodic collapse of the depression on the decane surface can be explained as follows: After the release of decane vapor/fragments into the gas phase, they start to absorb the incident laser energy, which reduces the laser flux reaching the decane surface. This reduction in the laser flux is significant for polymeric solids [8,9] and can be significant for decane. This reduces the amount of vaporization, which reduces the amount of depression.

The reduction in the amount of vaporization decreases the amount of decane vapor in the gas phase and the absorption of the laser energy decreases. More laser flux reaches the decane surface causing more vaporization and this cycle repeats periodically. Also, there may well be some effect of the flow motion in the decane caused by surface tension, and the collapse of the surface depression. The rapid outward radial movement shown in figure 5 was generated by surface waves and thereby the surface tension gradient caused by the steep temperature gradient along the radial direction [10,11]. This movement was confirmed by the rapid radial outward displacement of a small chip of plastic foam floating on the decane surface near the irradiated area. This flow removes part of the absorbed energy of the incident laser beam from the irradiated area. It also induces a convective upward flow from below to the irradiated area, satisfying the conservation of the mass. Therefore, the flow motion driven by a surface tension gradient can modify the amount of available energy for vaporization and the behavior of the surface depression.

The absorption characteristic of liquid decane in the region of the laser lines was determined by measurement of the absorption coefficient. Linear absorbance ($\log I_0/I$) was measured with a Perkin-Elmer Model 180 Infrared Photometer using a variable length cell from wavenumber 1100 to 800 cm^{-1} . Results are shown in figure 9 with various thicknesses of the cell. Absorption coefficients of liquid decane can be calculated as:

$$K = \frac{2.30}{\lambda} \log \frac{I_0}{I} \quad (2)$$

where ℓ is the thickness of the cell. However, figure 9 shows that the absorbance of the decane too sensitive to the wavenumber. Therefore, to obtain the absorption coefficient of decane, the fine structure of the emission spectrum of the CO₂ laser cannot be neglected. Then, the spectral average extinction coefficient becomes

$$\tilde{K} = \frac{1}{\ell} \ln \left[\frac{\int_{\nu_1}^{\nu_2} I_o(\lambda) d\lambda}{\int_{\nu_1}^{\nu_2} I_o(\lambda) e^{-K_\lambda \ell} d\lambda} \right] \quad (3)$$

the fine line structure of the emission spectrum of the CO₂ laser is shown in figure 10. Since the width of the laser lines is much narrower than those of the absorption bands, equation (3) can be written as

$$\tilde{K} = \frac{1}{\ell} \ln \left[\frac{\sum_{i=1}^n I_o(\lambda_i)}{\sum_{i=1}^n I_o(\lambda_i) e^{-K_{\lambda,i} \ell}} \right] \quad (4)$$

Using data from figure 9 and 10, the calculated absorption coefficient of liquid decane is 16 cm⁻¹ which is much smaller than about 90 cm⁻¹ for solid polystyrene [1]. Therefore, the laser beam can penetrate further into the decane. At 3 mm depth in the decane, the radiant flux is about 20 W/cm². With a smaller value of absorption coefficient for decane than that for solid polystyrene, the laser beam heats a larger volume of decane than of polystyrene. This is one of the reasons why decane requires a higher external radiant flux for ignition and its ignition delay time is longer than that of polystyrene at the same external radiant flux.

The relationship between the ignition delay time and the incident radiant flux was studied with various incident angles. Results are shown in figures 11a, b, and c. Although the relationship was measured at $\theta = 75^\circ$ and 60° , there was little difference among $\theta = 90^\circ$, $\theta = 75^\circ$ and $\theta = 60^\circ$. Results at $\theta = 75^\circ$ and 60° are not included since the plots are similar to figures 11 a-c. Roughly, when the incident radiant flux was below 2500 W/cm^2 , ignition delay time increased significantly with a further decrease in the incident radiant flux. A peculiar trend was noted. Ignition delay time appeared to increase slightly with the incident radiant flux for extremely high flux. This was observed at all five incident angles studied in this work. At present, it is not clear what mechanism causes this trend.

The effect of the incident laser beam angle on ignition delay time and the minimum incident radiant flux for ignition, I_{\min} , is clearly shown in figures 11 and 12. When the incident radiant flux is above roughly 2500 W/cm^2 , the effect of the incident laser beam angle on ignition delay time is not great. Ignition delay times at $\theta = 30^\circ$ are roughly 40% longer than those at $\theta = 90^\circ$. However, for incident radiant fluxes below 2500 W/cm^2 , this angle effect becomes significant with a large increase of ignition delay time found at the shallower incident beam angles. Also, the minimum incident radiant flux for ignition increases with a decrease in the incident laser angle. At $\theta = 90^\circ$ and 75° , $I_{\min} = 1000 \text{ W/cm}^2$. However, at $\theta = 60^\circ$, $I_{\min} = 1400 \text{ W/cm}^2$ and at $\theta = 45^\circ$, $I_{\min} = 1800 \text{ W/cm}^2$ and finally at $\theta = 30^\circ$, $I_{\min} = 2000 \text{ W/cm}^2$.

These trends of ignition delay time and the minimum incident radiant flux for ignition under various incident laser angles can be explained by:

1) the change of incident radiant flux distribution with incident angle of the laser beam to the decane surface; 2) the change of the absorption path length of the incident laser beam through the plume of decane vapor; 3) the change of the surface reflectance for the incident laser beam.

In the first mechanism, the actual incident radiant flux to the decane surface varies with the incident angle of the laser beam. At $\theta = 90^\circ$, the shape of the laser beam on the decane surface is equal to the normal radiant flux measured by the flux meter. However, at angles other than $\theta = 90^\circ$, the shape of the laser beam on the decane surface is ellipsoidal and the irradiated area increases with a decrease in the incident angle. This reduces the actual incident radiant flux per unit area. The relationship between the normal incident flux, I_o , and the actual incident flux, I , is

$$I = I_o \sin \theta$$

If this were the controlling mechanistic effect of the incident angle on the ignition, then for an $I_o = 1000 \text{ W/cm}^2$ at 90° , I_{\min} , should be 1150 W/cm^2 , 1400 W/cm^2 and 2000 W/cm^2 at $\theta = 60^\circ$, 45° and 30° respectively. These values are roughly 25% less than the measured results except at $\theta = 30^\circ$. At $\theta = 30^\circ$, the predicted and measured values agree. Nevertheless, the predicted trend, in which the minimum external normal radiant flux for ignition increases with decreasing incident angle, agrees with the observed one. However, the $\sin \theta$ correction does not explain the observed relationship between the ignition delay time and the actual incident flux, I . For example, in figure 12, the ignition delay time for an $I_o = 3000 \text{ W/cm}^2$ and $\theta = 30^\circ$ is about 90 msec. The actual incident flux I with $\sin 30^\circ$ would be 1500 W/cm^2 . However, the ignition delay time at $I_o = 1500 \text{ W/cm}^2$ and $\theta = 90^\circ$ is about 240 msec. Therefore,

the effect of the change in the incident radiant flux with the change in the incident angle can not explain completely the observed effects of the incident angles on ignition. However, this effect does describe fairly well the trend of the minimum radiant flux on ignition, in which the controlling process is apparently the heating of decane.

In the second mechanism, the interaction between the incident laser beam and decane vapor varies significantly with the incident angle of the laser beam. At $\theta = 90^\circ$, the direction of the jet like rising plume is the same as the incident laser beam and the interaction volume can be very large. However, decreasing the incident laser angle reduces the interaction volume significantly. Therefore, changing incident laser angle varies; 1) the total energy absorbed from the laser beam by decane vapor; 2) the rate of fuel vaporization due to the change in transmitted flux; 3) the residential flow time of decane vapor through the laser beam heated path. The net result of these changes on ignition varies for the same incident angle, depending on the energy flux in the laser beam. Under high incident flux and near vertical irradiation, the rate of vaporization is initially high. Due to the high fuel content of the jet like short plume, it absorbs strongly the laser energy and its temperature increases rapidly to ignition. Under high incident flux and oblique irradiation, the rate of vaporization is initially high. The interaction volume between the incident laser beam and the jet like short plume does not differ significantly from the near vertical irradiation and ignition occurs quickly due to the strong absorption of the laser beam.

At low incident radiant flux, the amount of decane vaporized becomes less and the concentration of decane vapor in the jet like plume becomes less.

At near vertical incident laser angles the absorbed energy from the incident laser beam is spread over the longer height of the jet like plume and the local absorbed intensity is correspondingly less. Although the local absorption is less, the total absorption may actually be more and the flux transmitted through the plume becomes less and the amount of decane vaporizing may be further reduced. Therefore, under low incident radiant flux, the large interaction volume at near vertical irradiation angles tends to delay ignition. At oblique incident laser angles, the incident flux to the decane surface through the smaller interaction volume does not decrease as much as at near vertical incident laser angles, thus the vaporization rate decreases less with time than for near vertical irradiation. This tends to favor early ignition, but the residential flow time of decane vapor through the heated gas layer by the absorption becomes less. For nearly vertical incident angles, the time for decane vapor to flow through the absorptively heated gas layer is long and eventually it becomes hot enough to trigger the ignition. For oblique incident laser angles decane vapor cuts diagonally across the heated gas layer and is heated only for a brief time. The long ignition delays for low incident flux and oblique incident angles reflect the long heating time required to raise the fuel vaporization rate sufficiently that there will be enough decane vapor in the plume to absorb laser energy and reach the high temperature before passing out of interaction volume. This mechanism introduces another parameter, the size of the laser beam, which was not varied in this study due to the lack of the laser power to maintain the same flux density over a larger area. If the size of the laser beam becomes larger, the irradiated area of the decane surface becomes larger and the plume of decane vapor becomes wider. The larger beam and

wider plume produce a larger interaction volume. Then, the residence time of a combustible mixture of gases moving through the interaction zone increases. Absorption of the laser beam energy increases with the longer residence time. Since the important condition for ignition is that the residence time must be longer than the gas phase chemical reaction time, the larger beam would reduce the minimum external radiant flux for ignition.

The third effect, the change in surface reflectance, is estimated by using Fresnel's equation with Snell's law. Although this estimation is only qualitative, it can show the trend of the effect of the incident angle on reflectance. The reflectance, R, against the decane surface, of the laser beam which has a polarization direction parallel to the plane of the incidence, can be written as: [12]

$$R = \left[\frac{\tan (\theta_i - \theta_t)}{\tan (\theta_i + \theta_t)} \right]^2 \quad (5)$$

where θ_i is the incident angle of the laser beam with respect to vertical line and θ_t is the transmitted angle. Therefore, the previously discussed θ is $\theta = 90^\circ - \theta_i$. By Snell's law,

$$n_i \sin \theta_i = n_t \sin \theta_t \quad (6)$$

where n_i is refractive index of the incident medium, air, and n_t is refractive index of the transmitted medium, decane. Although the value of the refractive index of decane at the visible wavelength is available and is 1.4, its value at the CO₂ laser wavelength (10.6 μm) is not available. From the study of Dalzell and Sarofim [13], it is expected that the value of refractive index at around 10.6 μm is larger than that at the visible wavelengths. Therefore, values of

reflectance at various incident angles were calculated with two different values of n_t , 1.4 and 2.8, using equations (5) and (6). Results are shown in figure 13. It shows that the qualitative trend of reflectance with the incident laser angle does not change with the value of refractive index. Reflectance decreases gradually with a decrease in the incident angle until about 20° for $n_t = 1.4$ and about 15° for $n_t = 2.8$. Then, reflectance increases sharply with a further decrease in the incident angle. Therefore, for the values of the incident angle used in this study ($\theta > 30^\circ$), the calculation shows qualitatively that more energy from the incident laser beam is transmitted into the decane with a decrease in the incident angle. This means that, if this mechanism controls the ignition processes, ignition delay time should decrease with a decrease in the incident angle. This trend is opposite from the one observed.

Ignition delay time was plotted against incident radiant flux in log-log coordinates to find any characteristic relationship between them. The plot is shown in figure 14. The relationship can be roughly expressed by the straight line, although the line shifts slightly at different incident laser angles. Also, near the minimum incident radiant flux for ignition, the relationship bends sharply upward deviating from the straight line. However, the slope of the straight line is fairly uniform from $\theta = 90^\circ$ to $\theta = 30^\circ$ and is about -1.6. This can be expressed as:

$$\tau \sim I_o^{-1.6}$$

This relationship can be used for rough prediction of the trend of ignition delay time with given incident radiant flux. The logarithmic plot between $I_o \sin \theta$ and ignition delay was not linearly correlated as well as the above log-log relationship.

4. THEORETICAL STUDY

A simplified theoretical model to describe the development of a plume in the gas phase was developed as a first step; hopefully, this will be extended to a more complete model which will be able to predict qualitatively the trends of ignition delay time and the minimum external radiant flux for ignition against various parameters such as flux, incident laser angle and laser beam diameter. As the key processes of the ignition mechanism are clarified experimentally, these will be added to improve the theoretical model. The model which is discussed in this section is a foundation for a more complete model and it emphasizes the gas phase. However, a similar approach can be extended to calculate the flow motion in the liquid phase. Two different approaches were used in this study, one is numerical and the other is analytical.

4.1 Numerical Study

A schematic illustration of the model is given in figure 15. The base is considered to be a solid and there is no motion inside of the solid. The enclosure is included artificially to define the boundary conditions. In the calculation, the enclosure is taken to be large enough so that the rising plume and the associated flow do not touch its walls. The flow is assumed to be axisymmetric and a cylindrical coordinate system with its origin at the center of a hot spot is used. The fluid is initially motionless and at a uniform temperature T_0 . The enclosure walls are also at this temperature, except for a small centrally located circular spot on the base of radius whose temperature increases with time as specified up to a temperature T_w . The temperature difference initiates and sustains a natural convection flow within the enclosure. The Boussinesq approximation is used; in this approximation density ρ

is assumed constant except for the generation of buoyancy forces. No chemical reaction and no mass addition are considered. Fluid properties are taken as constant; these include kinematic viscosity ν , thermal diffusively α , and volume expansion coefficient β . We introduce the following dimensionless quantities: time, $\tau = (\alpha/H^2)t$; initial and radial coordinates, $X = x/H$ and $R = r/H$; vertical and radial components of velocity, $U = (H/\alpha)u$ and $V = (H/\alpha)v$; and temperature $\theta = (T-T_0)/(T_w-T_0)$.

Introducing vorticity Ω and the stream function $\bar{\psi}$, the governing equations in dimensionless form are:

$$U = \frac{1}{R} \frac{\partial \bar{\psi}}{\partial R}, \quad V = -\frac{1}{R} \frac{\partial \bar{\psi}}{\partial X} \quad (5)$$

$$-\Omega = \frac{1}{R} \frac{\partial^2 \bar{\psi}}{\partial X^2} + \frac{2}{\partial R} \left(\frac{1}{R} \frac{\partial \bar{\psi}}{\partial R} \right) \quad (6)$$

$$\begin{aligned} \frac{\partial \Omega}{\partial C} + \left[\frac{\partial(U\Omega)}{\partial X} + \frac{\partial(V\Omega)}{\partial R} \right] &= -G_r P_r \frac{\partial^2 \theta}{\partial R} \\ &+ P_r \left[\frac{\partial^2 \Omega}{\partial X^2} + \frac{2}{\partial R} \left(\frac{1}{R} \frac{\partial \Omega}{\partial R} \right) \right] \end{aligned} \quad (7)$$

$$\text{and } \frac{\partial \theta}{\partial C} + \left[\frac{\partial(U\theta)}{\partial X} + \frac{1}{R} \frac{\partial(RV\theta)}{\partial R} \right] = \left[\frac{\partial^2 \theta}{\partial X^2} + \frac{1}{R} \frac{\partial}{\partial R} \left(\frac{R \partial \theta}{\partial R} \right) \right] \quad (8)$$

where

$$\Omega = \frac{\partial V}{\partial X} - \frac{\partial U}{\partial R} \quad (9)$$

Equation (7) contains the Prandtl number $\text{Pr} = \nu/\alpha$ and the Grashof number $\text{Gr} = g\beta(T_w - T_o)H^3/\nu^2$. The initial conditions are for $\tau < 0$

$$\Omega = \theta = 0 \quad 0 \leq X \leq 1 \text{ and } 0 \leq R \leq R_w \quad (10)$$

The boundary conditions for $\tau > 0$ are:

$$\left. \begin{array}{l} \bar{\Psi} = \frac{\partial \bar{\Psi}}{\partial X} = 0 \quad \text{for } X=0, 0 \leq R \leq R_w \\ \theta = 1 \quad \text{for } X=0, 0 \leq R \leq R_c \\ \theta = 0.5 \quad \text{for } X=0, R=R_c \\ \theta = 0 \quad \text{for } X=0, R_c < R \leq R_w \\ \bar{\Psi} = \frac{\partial \bar{\Psi}}{\partial X} = \theta = 0 \quad \text{for } X=1, \text{ all } R \\ \bar{\Psi} = \Omega = \frac{\partial \bar{\Psi}}{\partial R} = 0 \quad \text{for } R=0, \text{ all } X \\ \bar{\Psi} = \frac{\partial \bar{\Psi}}{\partial R} = \theta = 0 \quad \text{for } R=R_w, \text{ all } X \end{array} \right\} \quad (11)$$

The above equations are numerically solved using Torrance's computational programming [14,15]. The detailed calculation scheme is well described in these references.

The enlarged results near the heat source are shown in figures (16) and (17) for two different times. $G_r = 3.6 \times 10^5$ is derived from $H = 2.5 \text{ cm}$ and $T_w = 447^\circ\text{K}$. The physical time scales corresponding to $\tau = 2.1 \times 10^{-3}$

and $\tau = 7.0 \times 10^{-3}$ are about 60 msec and 210 msec, respectively. Since the enclosure boundary is at $X = 1$ and $R = 1$, the effect of the enclosure on the early development is negligible. At $\tau = 2.1 \times 10^{-3}$, heat transfer from the heated area to the surrounding gas phase is limited to near the source. Since thermal diffusion is the dominant transport process, the distance traveled by the energy at this time is about the same axially and radially. The sharp temperature gradient near the edge of the heated area is due to the room temperature boundary condition at the surface next to the heated area. The vorticity distribution indicates the initiation of strong vorticity near and over the edge of the heated area. Near the surface, the gradient of vorticity becomes steep due to the shear caused by the induced flow from the surroundings toward the heated plate. This steep gradient could reduce the accuracy of the calculation of vorticity near the surface unless the step size near the surface is very fine. The stream function clearly shows the flow pattern, in which hot air starts to rise and the surrounding air flows radially in toward the heated area. The effect of the heat input extends a greater distance in the flow pattern than in the temperature distribution due to the irrotational flow characteristic far from the heated area.

At $\tau = 7.0 \times 10^{-3}$, buoyancy starts to push the thermal wave further upward than does thermal diffusion and the temperature distribution is more elongated upwards than radially. The strong vorticity moves slightly more toward the center, where the shear becomes strong at the edge of the rising plume. The wall boundary grows further radially. The stream function distribution also shows enlargement of the flow motion. It is interesting to note that the stream lines are centered further away from the heated area than the center of the vorticity distribution. It indicates that, if decane vapor follows the

flow pattern, it can spread radially and it might be possible by this means to absorb enough energy from the incident laser beam to ignite. However, firm conclusions can only be derived from the future model including the liquid motion, vaporization and species equations in the gas phase.

4.2 Analytical Study

This model is basically the same as that of the numerical study. In this model, there is no enclosure and the gas phase is considered to be semi-infinite. Two-dimensional cartesian coordinates are used in this model for the simplification because of the possibility of extending it to more realistic three-dimensional coordinates.

Dimensionless variables are defined as follows:

$$\begin{aligned} U &= u/u_0, & V &= v/u_0 \\ X &= x/L & Y &= y/L \\ \tau &= t/T_0 & \theta &= \frac{T-T_0}{T_w-T_0} \end{aligned} \quad (12)$$

$$T_0 = \frac{L}{u_0}, \quad \mu = \frac{v}{L}$$

With $\text{Pr} = 1$, the governing equations become

$$\frac{\partial \Omega}{\partial \tau} + \frac{\partial U \Omega}{\partial X} + \frac{\partial V \Omega}{\partial Y} = \frac{\partial^2 \Omega}{\partial X^2} + \frac{\partial^2 \Omega}{\partial Y^2} + G_f \frac{\partial \theta}{\partial X} \quad (13)$$

$$\frac{\partial^2 \Psi}{\partial X^2} + \frac{\partial^2 \Psi}{\partial Y^2} = -\Omega \quad (14)$$

$$\frac{\partial \theta}{\partial \tau} + \frac{\partial U \theta}{\partial X} + \frac{\partial V \theta}{\partial Y} = \frac{\partial^2 \theta}{\partial X^2} + \frac{\partial^2 \theta}{\partial Y^2} \quad (15)$$

where $\Omega = \frac{\partial V}{\partial X} - \frac{\partial U}{\partial Y}$

$$\left. \begin{array}{l} U = \frac{\partial \Psi}{\partial Y} \\ V = -\frac{\partial \Psi}{\partial X} \end{array} \right\} \quad (16)$$

where $G_r = \frac{g\beta L^3(T_w - T_0)}{v^2}$

Initial conditions are

$$v = \bar{V} = \theta = \Omega = \Psi = 0 \quad \text{for all } X \text{ and } Y,$$

Boundary conditions for $\tau \geq 0$ are

$$\left. \begin{array}{l} \Omega = \theta = \frac{\partial \bar{\Psi}}{\partial X} = \frac{\partial \bar{\Psi}}{\partial Y} = 0 \quad \text{at } X=0 \text{ and } X=-L, \\ \Omega = \theta = \frac{\partial \bar{U}}{\partial X} = \frac{\partial \bar{U}}{\partial Y} = 0 \quad \text{at } Y=0 \\ \Psi = \frac{\partial \bar{\Psi}}{\partial X} = 0 \quad \text{at } Y=0 \text{ for all } X \\ \theta = 0 \quad \text{at } Y=0, |X| > \frac{1}{2} \\ \theta = 1 \quad \text{at } Y=0, |X| \leq \frac{1}{2} \end{array} \right\} \quad (17)$$

The order of the time dependency of each variable is analyzed to estimate the dominant terms for equations (13)-(15). Since the distance traveled by thermal diffusion, which initiates the flow motion, is roughly proportional to the square root of time

$$x \sim 0 (\sqrt{\tau})$$

Since the surface temperature does not change with time, $\theta \sim 0(1)$

In equation (13), the order of time dependency of the following two terms should be same because they are source and inertia terms.

$$\frac{\partial \Omega}{\partial \tau} \sim \frac{\partial \theta}{\partial X}$$

This can be satisfied if $\Omega \sim 0$ ($v\tau$).

Similarly, equation (16) indicates

$$U \sim V \sim 0 (\tau)$$

$$\bar{\Psi} \sim 0 (\tau^{3/2})$$

Substitute these order of time dependencies into equations (13)-(15),

$$\frac{\partial \Omega}{\partial \tau} + \underbrace{\frac{\partial U \Omega}{\partial X} + \frac{\partial V \Omega}{\partial Y}}_{O(\tau)} = \underbrace{\frac{\partial^2 \Omega}{\partial X^2} + \frac{\partial^2 \Omega}{\partial Y^2}}_{O(\tau^2)} + Gr \frac{\partial G}{\partial X}$$

$$\frac{\partial G}{\partial \tau} \quad O(\tau) \cdot O(\tau) \quad \frac{\partial G}{\partial \tau} \quad \frac{\partial G}{\partial \tau}$$

$$O(1/\tau) \quad O(\tau) \quad O(1/\tau) \quad O(1/\tau)$$

$$\underbrace{\frac{\partial^2 \bar{\Psi}}{\partial X^2} + \frac{\partial^2 \bar{\Psi}}{\partial Y^2}}_{O(\tau^{3/2})} = -\Omega$$

$$O(\tau^{3/2}) \quad O(\tau)$$

$$\frac{\partial \theta}{\partial \tau} + \underbrace{\frac{\partial U \theta}{\partial X} + \frac{\partial V \theta}{\partial Y}}_{O(\tau)} = \underbrace{\frac{\partial^2 \theta}{\partial X^2} + \frac{\partial^2 \theta}{\partial Y^2}}_{O(\tau^2)}$$

$$\frac{\partial \theta}{\partial \tau} \quad O(1/\tau) \cdot O(1) \quad \frac{\partial \theta}{\partial \tau}$$

$$O(1/\tau) \quad O(\tau) \quad O(1/\tau)$$

Therefore, all terms are same order with time except the convection terms. The ratio of the time dependency of the convection terms to the other terms is $O(\tau^{3/2})$. Therefore, if our interest is early time during the initiation of the plume, the convection terms can be neglected in this calculation. With $\tau = t/\tau_0$, we can estimate the time scale in which this calculation is reasonably accurate. Since U and V have a Grashof number dependence, the value of τ_0 must be evaluated on this basis instead of the one defined in equation (12).

$$\tau_0 = \frac{L}{U_0} \sim \frac{L}{\left(\frac{\Delta P}{\rho g L}\right)^{1/2}} \sim \frac{L}{\left(\frac{T_w - T_0}{T_w} \cdot g L\right)^{1/2}}$$

With the values of $L = 0.5$ cm and $T_w = 447^\circ K$, τ_0 is about 40 msec. With the ratio of $O(\tau^{3/2})$, the calculation is quantitatively accurate up to 20 msec ($\tau = 0.5$) and qualitatively accurate from 20 msec to 200 msec ($\tau \sim 1$).

The governing equations for the early time calculation are then

$$\frac{\partial Q}{\partial t} = \frac{\partial^2 Q}{\partial x^2} + \frac{\partial^2 Q}{\partial y^2} + G_f \frac{\partial G}{\partial x} \quad (18)$$

$$\frac{\partial^2 \Phi}{\partial x^2} + \frac{\partial^2 \Phi}{\partial y^2} = -Q \quad (19)$$

$$\frac{\partial G}{\partial t} = \frac{\partial^2 G}{\partial x^2} + \frac{\partial^2 G}{\partial y^2} \quad (20)$$

These equations with the boundary conditions described in equations (17) are linear and may be solved analytically. Another advantage of this approach is that the analytical procedure used here can be easily extended to the three dimensional case which might be difficult with the numerical calculation due to the requirement of large core size.

At first, equations (18)-(20) are converted by the Laplace transformation. The $\bar{\Omega}$, $\bar{\Psi}$ and $\bar{\theta}$ are variables of Ω , Ψ and θ after the Laplace transformation respectively.

$$P\bar{\Omega} - \left\{ \frac{\partial^2 \bar{\Omega}}{\partial x^2} + \frac{\partial^2 \bar{\Omega}}{\partial y^2} \right\} = G_r \frac{\partial \bar{\theta}}{\partial x} \quad (21)$$

$$\frac{\partial^2 \bar{\Psi}}{\partial x^2} + \frac{\partial^2 \bar{\Psi}}{\partial y^2} = -\bar{\Omega} \quad (22)$$

$$P\bar{\theta} - \left\{ \frac{\partial^2 \bar{\theta}}{\partial x^2} + \frac{\partial^2 \bar{\theta}}{\partial y^2} \right\} = 0 \quad (23)$$

where P is a variable for Laplace transformation. Then, the above equations are further converted by Fourier transformation with respect to the X coordinate. The $\bar{\Omega}$, $\bar{\Psi}$ and $\bar{\theta}$ are variables of $\bar{\Omega}$, $\bar{\Psi}$ and $\bar{\theta}$ after the Fourier transformation respectively.

$$\frac{\partial^2 \bar{\Omega}}{\partial y^2} - (\xi^2 + P)\bar{\Omega} = -G_r i \xi \bar{\theta} \quad (24)$$

$$\frac{\partial^2 \bar{\Psi}}{\partial y^2} - \xi^2 \bar{\Psi} = -\bar{\Omega} \quad (25)$$

$$\frac{\partial^2 \bar{\theta}}{\partial y^2} - (\xi^2 + P)\bar{\theta} = 0 \quad (26)$$

where ξ is a variable for the Fourier transformation.

Boundary conditions described in equation (17) are also converted as follows by Laplace transformation and Fourier transformation;

$$\left. \begin{aligned} \bar{\Omega} = \bar{\theta} = \frac{\partial \bar{\varphi}}{\partial Y} = 0 & \quad \text{for } Y=0 \\ \frac{\partial \bar{\varphi}}{\partial Y} = \bar{\varphi} = 0 & \quad \text{for } Y=0 \\ \bar{\theta} = \frac{1}{i\zeta p} \left(e^{\frac{i\zeta}{2}} - e^{-\frac{i\zeta}{2}} \right) & \quad \text{for } Y=0 \end{aligned} \right\} \quad (27)$$

The solution of equation (26) with equation (27) is

$$\bar{\theta} = \frac{\left(e^{\frac{i\zeta}{2}} - e^{-\frac{i\zeta}{2}} \right)}{i\zeta p} e^{-\sqrt{\zeta^2 + p^2} Y} \quad (28)$$

Similarly, solutions of equations (24) and (25) with equation (27) are

$$\bar{\Omega} = \frac{G_r}{P} \left(e^{\frac{i\zeta}{2}} - e^{-\frac{i\zeta}{2}} \right) \left[\left\{ \frac{1}{2\sqrt{p+\zeta^2} - i\zeta} - \frac{1}{p} \right\} \exp(-\sqrt{p+\zeta^2} Y) \right. \\ \left. + \frac{1}{2\sqrt{p+\zeta^2}} Y \exp(-\sqrt{p+\zeta^2} Y) \right] \quad (29)$$

$$\bar{\varphi} = \frac{G_r}{p^2} \left(e^{\frac{i\zeta}{2}} - e^{-\frac{i\zeta}{2}} \right) \left[\frac{e^{-i\zeta/Y}}{2\sqrt{p+\zeta^2}(\sqrt{p+\zeta^2} - i\zeta)} \right. \\ \left. - \frac{e^{-\sqrt{p+\zeta^2} Y}}{\sqrt{p+\zeta^2}(\sqrt{p+\zeta^2} - i\zeta)} - \frac{Y e^{-\sqrt{p+\zeta^2} Y}}{2\sqrt{p+\zeta^2}} \right] \quad (30)$$

The solution of the energy equation, equation (28), can be converted back by the Laplace transformation inversion [16].

$$\tilde{\theta} = \frac{Gr}{2\beta^2} (e^{\frac{i\beta Y}{2}} - e^{-\frac{i\beta Y}{2}}) \left\{ e^{-\frac{i\beta Y}{2}} \operatorname{erfc}\left(\frac{Y}{2\sqrt{T}} - i\sqrt{T}/\beta\right) \right. \\ \left. + e^{\frac{i\beta Y}{2}} \operatorname{erfc}\left(\frac{Y}{2\sqrt{T}} + i\sqrt{T}/\beta\right) \right\} \quad (31)$$

Using the contour integral, vorticity of equation (29) and stream function of equation (30) are converted back by the Laplace transformation inversion. Details of this inversion are described in Appendix A.

$$\tilde{\omega} = Gr (e^{\frac{i\beta Y}{2}} - e^{-\frac{i\beta Y}{2}}) \left[\left(\frac{3Y}{4\beta^2} + \frac{1}{8\beta^2 T} - T \right) e^{-\frac{i\beta Y}{2}} \cdot \operatorname{erfc}\left(\frac{Y}{2\sqrt{T}} - i\sqrt{T}/\beta\right) \right. \\ \left. - \left(\frac{T}{2} + \frac{Y}{2\beta^2} \right) e^{\frac{i\beta Y}{2}} \operatorname{erfc}\left(\frac{Y}{2\sqrt{T}} + i\sqrt{T}/\beta\right) - \frac{e^{-\frac{i\beta Y}{2}}}{8\beta^2} \operatorname{erfc}\left(\frac{Y}{2\sqrt{T}} + i\sqrt{T}/\beta\right) \right. \\ \left. + \frac{i\sqrt{T}}{4+T/\beta^2} e^{-\frac{i\beta Y}{2} - \frac{Y^2}{4T}} \right] \quad (32)$$

$$\tilde{\psi}_H = \frac{Gr}{16\beta^2} (e^{\frac{i\beta Y}{2}} - e^{-\frac{i\beta Y}{2}}) e^{-\frac{i\beta Y}{2}} \left\{ (4T - 4T\beta^2 - \frac{3}{\beta^2}) \operatorname{erfc}(i\sqrt{T}/\beta) \right. \\ \left. - \frac{2\sqrt{T}}{T\beta^2} e^{-\frac{\beta^2 T}{2} \left(2T/\beta^2 - \frac{3}{\beta^2} \right)} \right\}$$

$$\tilde{\Psi}_p = \frac{Gr}{\xi^2} (e^{-\frac{\xi^2}{2}} - e^{-\frac{\xi^2}{2}}) \left[-\frac{1}{18\xi^2} \left(e^{-\frac{1}{3}\gamma Y} \operatorname{erfc}\left(\frac{Y}{2\sqrt{\gamma}} - i\sqrt{\gamma}\xi\right) \right) \right]$$

$$\left\{ -4T - 2(2T|\xi| - Y)^2 + \frac{4}{|\xi|} (2T|\xi| - Y) - \frac{3}{\xi^2} \right\}$$

$$+ 2\sqrt{\frac{T}{\pi}} e^{-\frac{\xi^2}{2} - \frac{Y^2}{4T}} \left(-4T|\xi| + 2Y + \frac{6}{|\xi|} \right) + e^{\frac{Y|\xi|}{2\sqrt{\gamma}}} \operatorname{erfc}\left(\frac{Y}{2\sqrt{\gamma}} + i\sqrt{\gamma}|\xi|\right)$$

$$\left\{ -\frac{2}{|\xi|} (2T|\xi| + Y) + \frac{3}{\xi^2} \right\} - \frac{Y}{4\xi^2} \left[e^{-\frac{1}{3}\gamma Y} \operatorname{erfc}\left(\frac{Y}{2\sqrt{\gamma}} - i\sqrt{\gamma}|\xi|\right) \right]$$

$$\begin{aligned} & \left(\frac{1}{|\xi|} - 2T|\xi| + Y \right) + e^{\frac{1}{3}\gamma Y} \operatorname{erfc}\left(\frac{Y}{2\sqrt{\gamma}} + i\sqrt{\gamma}|\xi|\right) \left(-\frac{1}{|\xi|} + 2T|\xi| + Y \right) \\ & - 4\sqrt{\frac{T}{\pi}} e^{-\frac{\xi^2}{2} - \frac{Y^2}{4T}} \end{aligned} \quad (33)$$

where $\tilde{\Psi}_H$ is the homogenous solution and $\tilde{\Psi}_p$ the particular solution.

The next step is the Fourier transformation inversion of solutions described in equations (31)-(33). For example,

$$\theta(x, Y, T) = \frac{1}{2\pi} \int_{-\infty}^{\infty} e^{i\xi x} \tilde{\theta} d\xi \quad (34)$$

$$\tilde{\theta} = \frac{Gr}{\xi} \cdot \frac{e^{\frac{\xi^2}{2}} - e^{-\frac{\xi^2}{2}}}{2i} \cdot f(|\xi|, Y, T) = Gr \cdot \frac{\sin \frac{\xi}{2}}{\xi} f(|\xi|, Y, T)$$

Then, equation (34) becomes

$$\begin{aligned} \theta &= \frac{Gr}{2\pi} \int_{-\infty}^{\infty} \frac{\sin \frac{\xi}{2}}{\xi} \left\{ \cos(\xi x) + i \sin(\xi x) \right\} f(|\xi|, Y, T) d\xi \\ &= \frac{Gr}{\pi} \int_0^{\infty} \frac{\sin \frac{\xi}{2}}{\xi} \cos(\xi x) f d\xi \\ &= \frac{Gr}{2\pi} \int_0^{\infty} \frac{1}{\xi} \left\{ \sin \xi \left(\frac{1}{2} - x\right) + \sin \xi \left(\frac{1}{2} + x\right) \right\} \\ &\quad \left\{ e^{-\frac{\gamma Y}{2}} \operatorname{erfc}\left(\frac{Y}{2} - \xi\right) + e^{\frac{\gamma Y}{2}} \operatorname{erfc}\left(\frac{Y}{2} + \xi\right) \right\} \frac{d\xi}{\sqrt{\gamma}} \end{aligned}$$

where

$$\sqrt{\gamma}|\xi| = \xi \quad , \quad \gamma = \frac{Y}{T} \quad (35)$$

Defining

$$\lambda_1 = \frac{\frac{1}{2} - X}{\sqrt{C}} \quad \text{and} \quad \lambda_2 = \frac{\frac{1}{2} + X}{\sqrt{C}} \quad (36)$$

$$\begin{aligned} \theta &= \frac{Gr}{2\pi} \left[\int_0^\infty \sin(\lambda_1 s) \frac{1}{s} \left\{ e^{-\frac{3s}{2}} \operatorname{erfc}\left(\frac{s}{2} - \xi\right) + e^{\frac{3s}{2}} \operatorname{erfc}\left(\frac{s}{2} + \xi\right) \right\} ds \right. \\ &\quad \left. + \int_0^\infty \sin(\lambda_2 s) \frac{1}{s} \left\{ e^{-\frac{5s}{2}} \operatorname{erfc}\left(\frac{s}{2} - \xi\right) + e^{\frac{5s}{2}} \operatorname{erfc}\left(\frac{s}{2} + \xi\right) \right\} ds \right] \end{aligned} \quad (37)$$

Similarly, vorticity becomes

$$\begin{aligned} \Omega &= -\frac{Gr}{\pi} \int_{-\infty}^{\infty} \sin \frac{\xi}{2} \sin(3X) g(1/\xi) d\xi \\ &= -\frac{Gr}{\pi} \int_0^\infty \left\{ \cos \frac{\xi}{2} \left(\frac{1}{2} - X \right) - \cos \frac{\xi}{2} \left(\frac{1}{2} + X \right) \right\} g(1/\xi) d\xi \\ &= -\frac{Gr\sqrt{C}}{\pi} \left[\int_0^\infty \cos(\lambda_1 s) \cdot \frac{1}{s} \left\{ \left(\frac{3}{4}s + \frac{1}{8s} - \xi \right) e^{-\frac{3s}{2}} \operatorname{erfc}\left(\frac{s}{2} - \xi\right) \right. \right. \\ &\quad \left. \left. - \frac{1}{2}(s+1) e^{\frac{3s}{2}} \operatorname{erfc}\left(\frac{s}{2} + \xi\right) - \frac{e^{-\frac{5s}{2}}}{8s} \operatorname{erfc}\left(\frac{s}{2} + \xi\right) + \frac{1}{4\sqrt{C}} e^{-\frac{5s^2}{4}} \right\} ds \right] \\ &\quad - \int_0^\infty \cos(\lambda_2 s) \cdot \frac{1}{s} \left\{ \left(\frac{3}{4}s + \frac{1}{8s} - \xi \right) e^{-\frac{5s}{2}} \operatorname{erfc}\left(\frac{s}{2} - \xi\right) \right. \\ &\quad \left. - \frac{1}{2}(s+1) e^{\frac{5s}{2}} \operatorname{erfc}\left(\frac{s}{2} + \xi\right) - \frac{e^{-\frac{3s}{2}}}{8s} \operatorname{erfc}\left(\frac{s}{2} + \xi\right) + \frac{1}{4\sqrt{C}} e^{-\frac{3s^2}{4}} \right\} ds \end{aligned} \quad (38)$$

Also, homogenous and particular solutions for the stream function become

$$\begin{aligned} \bar{\Psi}_H &= -\frac{Gr}{16\pi} \int_{-\infty}^{\infty} \sin \frac{\xi}{2} \sin(3X) H(1/\xi, Y, C) d\xi \\ &= -\frac{Gr}{16\pi} \int_0^\infty \left\{ \cos \frac{\xi}{2} \left(\frac{1}{2} - X \right) - \cos \frac{\xi}{2} \left(\frac{1}{2} + X \right) \right\} H(1/\xi, Y, C) d\xi \end{aligned}$$

$$= \frac{-\pi}{16R} T^{1/2} \int_0^\infty \frac{1}{5s^2} \{ \cos(\lambda_1 s) - \cos(\lambda_2 s) \} e^{-\frac{s^2}{4}} \{ (4 - 4s^2$$

$$- \frac{3}{s^2}) \operatorname{erf}(s) - \frac{2}{\pi} (2s - \frac{3}{s}) e^{-\frac{s^2}{4}} \} ds \quad (39)$$

$$\begin{aligned} \bar{\Psi}_P &= - \frac{Gr}{8\pi} \int_{-\infty}^0 \sin \frac{\xi}{2} \sin(\xi x) K(1/3, \sqrt{T}) d\xi \\ &= - \frac{Gr}{8\pi} \int_0^\infty \{ \cos s(\frac{1}{2} - x) - \cos s(\frac{1}{2} + x) \} K(1/3, \sqrt{T}) ds \\ &= - \frac{(GrT)^{1/2}}{8\pi} \int_0^\infty \{ \cos(\lambda_1 s) - \cos(\lambda_2 s) \} \{ (3 + (2s - \frac{1}{2}))^2 - \frac{2(2s+1)}{s} \} \\ &\quad + \frac{3}{2s^2} \left\{ e^{-\frac{s^2}{4}} \operatorname{erfc}\left(\frac{1}{2} - s\right) + (-4s + 2) + \frac{6}{s} \right\} \frac{1}{\pi R} e^{-\frac{s^2}{4}} ds \\ &\quad + \left\{ -\frac{(2s+1)}{s} + \frac{3}{2s^2} \right\} e^{-\frac{s^2}{4}} \operatorname{erfc}\left(\frac{1}{2} + s\right) - 4 \left\{ \left(\frac{1}{s} - 2s + \frac{1}{2}\right) e^{-\frac{s^2}{4}} \right. \\ &\quad \cdot \operatorname{erfc}\left(\frac{1}{2} - s\right) + \left(-\frac{1}{s} + 2s + 1\right) e^{-\frac{s^2}{4}} \operatorname{erfc}\left(\frac{1}{2} + s\right) \\ &\quad \left. - \frac{4}{\pi} e^{-\frac{s^2}{4} - \frac{11}{4}} \right\} \} ds \end{aligned} \quad (40)$$

At present, the integration of equations (37)–(40) has not been completed.

There is some chance that these may be integrated analytically. Even if numerical integration is required, these are single integrals and can be carried out without any difficulty and with small computation time. These solutions will reflect the effects from the two source terms with $\sin(\lambda_1 \zeta)$ and $\sin(\lambda_2 \zeta)$ or $\cos(\lambda_1 \zeta)$ and $\cos(\lambda_2 \zeta)$ describing the disturbance generated around the edges of the heated base. The λ_1 and λ_2 express the distance from the sources to the observation point. Values of all terms except $\bar{\Psi}_H$ decreases

very rapidly away from these sources and this makes the numerical integration easy without integrating far out in the field.

5. SUMMARY

The ignition mechanism of n-decane was studied experimentally by using a CW CO₂ laser as an external radiant source; a simplified theoretical model to describe the development of a plume in the gas phase was developed as a first step.

From the experimental study of the effect of the container size on ignition delay time, it was concluded that a container with 6 cm diameter and 5 cm depth is sufficient to avoid any significant effect of the wall on ignition for a beam of the diameter used in these experiments.

High speed motion pictures show the periodic appearance and collapse of a bubble-like, half spherical surface depression near the surface. The depression is probably formed by the momentum of decane vapor leaving the decane surface and its collapse is caused by the absorption of the laser beam by the decane vapor in the gas phase reducing the energy available to vaporize liquid decane. Further studies are necessary to confirm these proposed mechanisms and to clarify the transport processes of decane vapor/droplets from the surface to the location in the gas phase where the first appearance of flame is observed.

The effect on ignition delay time of incidence angle of the laser beam on the decane surface is significant at low incident radiant flux. A decrease in the incident angle tends to increase ignition delay time and the minimum incident radiant flux for ignition. However, when the incident flux is above 2500 W/cm², this effect is not significant for the range of incident angles studied in this work.

It is concluded that the key mechanism in the ignition of decane by a CO₂ laser is the absorption of the laser beam energy by the decane vapor in the gas phase. The characteristic relationship between ignition delay time and incident radiant flux can be expressed by $\tau \sim I_0^{-1.6}$ from $\theta = 90^\circ$ to $\theta = 30^\circ$.

The theoretical model to describe the development of a plume in the gas phase caused by a heated surface was solved numerically and analytically. Further improvements including the addition of liquid vaporization, mass addition into the gas phase, species equations, absorption of laser beam energy and chemical reaction are necessary to complete the model. These will be carried out step-by-step with the numerically solved model. The analytical solution for the early time behavior is derived by using the Laplace transformation with respect to time and the Fourier transformation with respect lateral coordinates. However, further numerical calculation of the solution in the integral formual is necessary to complete the analytical model.

6. REFERENCES

- [1] Ohlemiller, T. J. and Summerfield, M., "Radiative Ignition of Polymeric Materials in Oxygen/Nitrogen Mixtures", Thirteenth Symposium (International) on Combustion, Combustion Institute, 1971, pp. 1087-1094.
- [2] Stegman, R. L., Schriempf, J. T., and Hettche, L. R., "Experimental Studies of Laser - Supported Absorption Waves with 5 ms Pulses of 10.6μ Radiation", J. Appl. Phys., Vol. 44, 1973, pp. 3675-3681.
- [3] Chien, K. Y., "Vaporization of Liquid-Air Droplets by High-Power Laser Beams", AIAA J., 1975, pp. 1647-1652.
- [4] Emmony, D. C., "High Speed Study of Laser-Liquid Interaction", J. Photo. Sci., 1977, pp. 41-44.
- [5] Handbook of Tables for Applied Engineering Science, CRC Press, Cleveland, Ohio, 1973.
- [6] Weast, R. C., Handbook of Chemistry and Physics, The Chemical Rubber Company, 1969.
- [7] Kashiwagi, T., "Effect of Sample Orientation on Radiative Ignition of Solid Fuel", to be submitted to Combustion and Flame.
- [8] Kashiwagi, T., "Experimental Observation of Radiative Ignition Mechanisms", Combustion and Flame, 34, 231 (1979).

- [9] Kashiwagi, T., "Effect of Attenuation of Radiation on Surface Temperature for Radiative Ignition", accepted for publication in Combustion Science and Technology.
- [10] MacKinven, R., Hansel, J. G. and Glassman, I., "Influence of Laboratory Parameters on Flame Spread Across Liquid Fuels", Comb. Sci. Tech. 1, 1979, pp. 293.
- [11] Murad, R. J., Lamendola, J., Isoda, H. and Summerfield, M., "A Study of Some Factors Influencing the Ignition of a Liquid Pool", Comb. Flame, 15, 1979, pp. 293.
- [12] Jackson, J. D., "Classical Electrodynamics", John Wiley and Sons, Inc., New York, Chap. 7, 1962.
- [13] Dalzell, W. H. and Sarofim, A. F., "Optical Constants of Soot and Thin Application to Heat-Flux Calculations", J. Heat Transfer, 91, 100 (1961).
- [14] Torrance, K. E., "Comparison of Finite-Difference Computations of Natural Convection", J. Research of National Bureau of Standards, B. Mathematical Sciences, 72B, 281 (1968).
- [15] Torrance, K. E. and Rockett, J. A., "Numerical Study of Natural Convection in an Enclosure with Localized Heating from Below - Creeping Flow to the Onset of Laminar Instability", J. Fluid Mech., 36, 33 (1969).
- [16] Carslaw, H. S. and Jaeger, J. C., "Conduction of Heat in Solids", Oxford Univ. Press, 496 (1965).

LIST OF FIGURES

1. Schematic illustration of experimental apparatus.
2. Picture of experimental apparatus
A - CO₂ laser, B - mirror, C - mirror, D - chamber, E - safety shield
3. The effect of the container depth on ignition delay time.
4. The effect of the container diameter on ignition delay time.
 - (a) $I_o = 4170 \pm 100 \text{ W/cm}^2$, (b) $I_o = 1670 \pm 80 \text{ W/cm}^2$
5. High speed motion pictures
 $I_o = 2200 \text{ W/cm}^2$, $\theta = 30^\circ$
 - (a) before laser irradiation, (b) 28 msec after laser irradiation,
 - (c) 72 msec, (d) 117 msec, (e) 340 msec, shortly after ignition,
 - (f) 370 msec
6. High speed motion pictures. $I_o = 3000 \text{ W/cm}^2$, $\theta = 30^\circ$
7. High speed motion pictures (negative). $I_o = 2000 \text{ W/cm}^2$, $\theta = 90^\circ$
8. High speed schlieren pictures. $I_o = 2600 \text{ W/cm}^2$, $\theta = 90^\circ$.
knife edge is horizontal direction.
9. Spectra of linear absorbance of decane
 - (a) cell only, (b) $\ell = 0.1$, (c) $\ell = 0.25$, (d) $\ell = 0.5$, (e) $\ell = 0.75$ and (f) $\ell = 1.0 \text{ mm}$.
10. Emission spectra of the CO₂ laser.
11. The relationship between incident radiant flux and ignition delay time under various incident angles. (a) $\theta = 90^\circ$, (b) $\theta = 45^\circ$, (c) $\theta = 30^\circ$.

12. The relationship between incident angle and ignition delay time under various incident radiant fluxes.
13. The calculated relationship between reflectance and incident angle.
14. The logarithmic relationship between ignition delay time and incident radiant flux.
15. A schematic illustration of the theoretical model.
16. Computational results of early development of plume at $\tau = 2.1 \times 10^{-3}$, $Gr = 3.6 \times 10^5$, $Pr = 0.7$. (a) temperature, (b) vorticity and (c) stream function.
17. Computational results of early development of plume at $\tau = 7.0 \times 10^{-3}$, $Gr = 3.6 \times 10^5$, $Pr = 0.7$. (a) temperature, (b) vorticity and (c) stream function.

1. *Leucanthemum vulgare* L. (L.)

2. *Leucanthemum vulgare* L. (L.)

3. *Leucanthemum vulgare* L. (L.)

4. *Leucanthemum vulgare* L. (L.)

5. *Leucanthemum vulgare* L. (L.)

6. *Leucanthemum vulgare* L. (L.)

7. *Leucanthemum vulgare* L. (L.)

8. *Leucanthemum vulgare* L. (L.)

9. *Leucanthemum vulgare* L. (L.)

10. *Leucanthemum vulgare* L. (L.)

11. *Leucanthemum vulgare* L. (L.)

12. *Leucanthemum vulgare* L. (L.)

13. *Leucanthemum vulgare* L. (L.)

14. *Leucanthemum vulgare* L. (L.)

15. *Leucanthemum vulgare* L. (L.)

16. *Leucanthemum vulgare* L. (L.)

17. *Leucanthemum vulgare* L. (L.)

18. *Leucanthemum vulgare* L. (L.)

19. *Leucanthemum vulgare* L. (L.)

20. *Leucanthemum vulgare* L. (L.)

21. *Leucanthemum vulgare* L. (L.)

22. *Leucanthemum vulgare* L. (L.)

23. *Leucanthemum vulgare* L. (L.)

24. *Leucanthemum vulgare* L. (L.)

25. *Leucanthemum vulgare* L. (L.)

26. *Leucanthemum vulgare* L. (L.)

27. *Leucanthemum vulgare* L. (L.)

28. *Leucanthemum vulgare* L. (L.)

29. *Leucanthemum vulgare* L. (L.)

30. *Leucanthemum vulgare* L. (L.)

APPENDIX A

The calculation of the Laplace transformation inversion for vorticity and stream function is described in this appendix.

From equation (29),

$$\bar{\Omega} = \text{Gr} \left(e^{\frac{Y}{2}} - e^{-\frac{Y}{2}} \right) \left[\frac{e^{-\sqrt{P+\frac{S^2}{3}}} Y}{2P\sqrt{P+\frac{S^2}{3}}(\sqrt{P+\frac{S^2}{3}} - \frac{S}{3})} - \frac{1}{P^2} e^{-\sqrt{P+\frac{S^2}{3}}} Y \right. \\ \left. + \frac{Y}{2P\sqrt{P+\frac{S^2}{3}}} e^{-\sqrt{P+\frac{S^2}{3}}} Y \right] \quad (A-1)$$

The first term in the above bracket is defined as

$$f_1(P) = \frac{e^{-\sqrt{P+\frac{S^2}{3}}} Y}{2P\sqrt{P+\frac{S^2}{3}}(\sqrt{P+\frac{S^2}{3}} - \frac{S}{3})} \quad (A-2)$$

The Laplace inversion of

$$f(P), \mathcal{L}\{f(P)\}$$

$$\mathcal{L}^{-1}\{f(P)\} = \frac{1}{2\pi i} \int_{\gamma-i\infty}^{\gamma+i\infty} e^{pt} f(p) dp$$

Define

$$P + \frac{S^2}{3} = s$$

$$\mathcal{L}^{-1}\{f_1(P)\} = \frac{e^{-\frac{S^2}{3}t}}{4\pi i} \int_{R-i\infty}^{R+i\infty} \frac{e^{st-\sqrt{s}Y}}{\sqrt{s}(s+\frac{S}{3})(s-\frac{S}{3})^2} ds \quad (A-3)$$

After the contour integral, which has a branch cut along the negative real coordinate from the origin, equation (A-3) becomes

$$\mathcal{L}^{-1}\{f_1(P)\} = -\frac{e^{-\frac{S^2}{3}t}}{4\pi} \int_0^\infty \frac{e^{-8t}}{18(s+\frac{S^2}{3})^2} \left\{ \frac{S}{3} (e^{i\sqrt{8}Y} - e^{-i\sqrt{8}Y}) - i\bar{S} (e^{i\sqrt{8}Y} - e^{-i\sqrt{8}Y}) \right\} ds$$

$$= e^{-\frac{\zeta^2}{2T}} \left[\frac{1}{4\pi} \int_0^\infty \frac{e^{-\zeta z}}{(z+\xi^2)^2} (e^{iz^2} - e^{-iz^2}) dz - \frac{i\xi}{4\pi} \int_0^\infty \frac{e^{-\zeta z}}{z(z+\xi^2)^2} (e^{iz^2} + e^{-iz^2}) dz \right]$$

Let $Z = U^2$

$$\begin{aligned} \mathcal{L}^{-1}\{f_1(p)\} &= e^{-\frac{\zeta^2}{2T}} \left[\frac{1}{2\pi} \int_{-\infty}^0 \frac{e^{-\zeta u+i\pi/4}}{(u+\xi^2)^2} du - \frac{i\xi}{2\pi} \int_{-\infty}^0 \frac{e^{-\zeta u-i\pi/4}}{(u+\xi^2)^2} du \right] \\ &= \frac{e^{-\frac{\zeta^2}{2T}}}{8\pi|\xi|} \int_{-\infty}^0 e^{-\zeta u+i\pi/4} \left[\frac{2}{(u-i\xi)^2} - \frac{1}{i\xi(u-i\xi)} + \frac{1}{i\xi(u+i\xi)} \right] du \\ &= \frac{e^{-\frac{\zeta^2}{2T}}}{8\pi|\xi|} \left\{ -2\pi f(2\pi|\xi| - Y) e^{(\zeta\xi^2 - Y|\xi|)} \operatorname{erfc}\left(\frac{Y}{2\sqrt{T}} - i\zeta|\xi|\right) \right. \\ &\quad \left. + \frac{2\sqrt{T}}{\sqrt{\pi}} e^{-\frac{Y^2}{4T}} \right\} - \frac{1}{i\xi} (-\pi i) e^{(\zeta\xi^2 - Y|\xi|)} \operatorname{erfc}\left(\frac{Y}{2\sqrt{T}} - i\zeta|\xi|\right) \\ &\quad + \frac{1}{i\xi} (-\pi i) e^{(\zeta\xi^2 - Y|\xi|)} \operatorname{erfc}\left(\frac{Y}{2\sqrt{T}} + i\zeta|\xi|\right) \Big] \\ &= \frac{e^{-\frac{\zeta^2}{2T}}}{8|\xi|} \left\{ -2f(2\pi|\xi| - Y) e^{(\zeta\xi^2 - Y|\xi|)} \cdot \operatorname{erfc}\left(\frac{Y}{2\sqrt{T}} - i\zeta|\xi|\right) \right. \\ &\quad \left. + \frac{2\sqrt{T}}{\sqrt{\pi}} e^{-\frac{Y^2}{4T}} \right\} + \frac{1}{|\xi|} e^{(\zeta\xi^2 - Y|\xi|)} \cdot \operatorname{erfc}\left(\frac{Y}{2\sqrt{T}} - i\zeta|\xi|\right) \\ &\quad - \frac{1}{|\xi|} e^{(\zeta\xi^2 - Y|\xi|)} \operatorname{erfc}\left(\frac{Y}{2\sqrt{T}} + i\zeta|\xi|\right) \Big] \quad (A-4) \end{aligned}$$

By Carslaw and Jaeger [16],

$$\mathcal{L}^{-1} \left\{ \frac{e^{-\sqrt{P+\beta^2}Y}}{P^2} \right\} = \frac{1}{2} \left\{ \left(T - \frac{Y}{2\beta} \right) e^{-\frac{Y\beta}{2T}} \operatorname{erfc} \left(\frac{Y}{2T} + \sqrt{T}\beta \right) \right. \\ \left. + \left(T + \frac{Y}{2\beta} \right) e^{-\frac{Y\beta}{2T}} \operatorname{erfc} \left(\frac{Y}{2T} - \sqrt{T}\beta \right) \right\} \quad (A-5)$$

Also,

$$\mathcal{L}^{-1} \left\{ \frac{e^{-\sqrt{P+\beta^2}Y}}{P\sqrt{P+\beta^2}} \right\} = \frac{1}{2\beta} \left\{ e^{-\frac{Y\beta}{2T}} \operatorname{erfc} \left(\frac{Y}{2T} - \sqrt{T}\beta \right) \right. \\ \left. - e^{-\frac{Y\beta}{2T}} \operatorname{erfc} \left(\frac{Y}{2T} + \sqrt{T}\beta \right) \right\} \quad (A-6)$$

Equation (32) can be derived by substituting equations (A-4), (A-5) and (A-6) into equation (A-1),

For stream function, from equation (30),

$$\bar{\Psi} = \frac{G\Gamma}{2} \left(e^{\frac{\beta Y}{2}} - e^{-\frac{\beta Y}{2}} \right) \left\{ \frac{e^{-\frac{Y\beta}{2T}}}{P^2\sqrt{P+\beta^2}(\sqrt{P+\beta^2}-\beta)} \right. \\ \left. - \frac{e^{-\sqrt{P+\beta^2}Y}}{P^2\sqrt{P+\beta^2}(\sqrt{P+\beta^2}+\beta)} - \frac{Ye^{-\sqrt{P+\beta^2}Y}}{P^2\sqrt{P+\beta^2}} \right\} \quad (A-7)$$

$$\mathcal{L}^{-1} \{ f_2(P) \} = \mathcal{L}^{-1} \left\{ \frac{e^{-\sqrt{P+\beta^2}Y}}{P^2\sqrt{P+\beta^2}(\sqrt{P+\beta^2}+\beta)} \right\}$$

With $P+\beta^2=S$

$$\mathcal{L}^{-1} \{ f_2(P) \} = \frac{1}{2\pi i} \int_{R-i\infty}^{R+i\infty} \frac{e^{S\Gamma-\beta Y}}{IS(\frac{1}{2}S+1)^2(\frac{1}{2}S+1)^3} ds$$

After the contour integral which is same contour as that of the vorticity,

$$\mathcal{L}^{-1}\{f_2(p)\} = \frac{e^{-\xi^2 T}}{2\pi i} \int_{\gamma-i\infty}^{\gamma+i\infty} \frac{e^{-st}}{\sqrt{s}(s+\xi^2)^3} \left[\frac{1}{3} (e^{i\pi/3} + e^{-i\pi/3}) - i\sqrt{3} (e^{i\sqrt{3}sY} - e^{-i\sqrt{3}sY}) \right] ds$$

Let $u^2 = s$

$$\begin{aligned} \mathcal{L}^{-1}\{f_2(p)\} &= \frac{e^{-\xi^2 T}}{\pi} \left\{ \frac{1}{3} \int_{-\infty}^{\infty} \frac{e^{-u^2 T + iuY}}{(u+\xi^2)^3} du - i \int_{-\infty}^{\infty} \frac{e^{-u^2 T + iuY}}{(u+\xi^2)^3} u du \right\} \\ &= \frac{e^{-\xi^2 T}}{16\pi\xi^2} \int_{-\infty}^{\infty} e^{-u^2 T + iuY} \left\{ \frac{4T}{(u-i/3)^3} - \frac{4}{1/3(u-i/3)^2} - \frac{3i}{3(u-i/3)} \right. \\ &\quad \left. - \frac{2}{1/3(u+i/3)^2} + \frac{3i}{3^2(u+i/3)} \right\} du \\ &= \frac{1}{16\xi^2} \left[e^{-Y/3} \operatorname{erfc}\left(\frac{Y}{2\sqrt{T}} - i\sqrt{T}/3\right) \left\{ -4T - 2(2T/3 + Y)^2 + \frac{4(2T/3 + Y)}{1/3} \right. \right. \\ &\quad \left. \left. - \frac{3}{3^2} \right\} + \frac{2\sqrt{T}}{\sqrt{\pi}} e^{-\xi^2 T - \frac{Y^2}{4T}} \left(-4T/3 + 2Y + \frac{6}{1/3} \right) \right. \\ &\quad \left. + e^{1/3^2 Y} \operatorname{erfc}\left(\frac{Y}{2\sqrt{T}} + i\sqrt{T}/3\right) \left\{ -\frac{2}{1/3} (2T/3 + Y) + \frac{3}{3^2} \right\} \right] \quad (A-8) \end{aligned}$$

$$\mathcal{L}^{-1}\{f_3(p)\} = \mathcal{L}^{-1}\left\{ \frac{Y e^{-i\sqrt{p+\xi^2} Y}}{p^2 \sqrt{p+\xi^2}} \right\}$$

Similar to the previous case, with $p+\xi^2 = s$

$$\mathcal{L}^{-1}\{f_3(p)\} = \frac{Y}{2\pi i} e^{-\xi^2 T} \int_{R-i\infty}^{R+i\infty} \frac{e^{st-i\sqrt{s}Y}}{\sqrt{s}(\sqrt{s}-1/3)^2(\sqrt{s}+1/3)^2} ds$$

After the contour integral,

$$\mathcal{L}^{-1}\{f_3(p)\} = \frac{Y e^{-\xi^2 T}}{2\pi C} \int_{-\infty}^{\infty} \frac{e^{-\xi T} (e^{i\xi x} + e^{-i\xi x})}{\pi \xi (x+\xi^2)^2} dx$$

Let $\xi = u^2$,

$$\begin{aligned} \mathcal{L}^{-1}\{f_3(p)\} &= -\frac{Y e^{-\xi^2 T}}{R} \int_0^\infty \left[\frac{e^{-u^2 T+iuy}}{(u^2+\xi^2)^2} + \frac{e^{-u^2 T-iuy}}{(u^2+\xi^2)^2} \right] du \\ &= \frac{Y e^{-\xi^2 T}}{4\pi \xi^2} \int_{-i\infty}^{i\infty} e^{-u^2 T+iuy} \left\{ \frac{1}{(u-i\xi)^2} - \frac{1}{(u+i\xi)^2} \right\} du \end{aligned}$$

$$\begin{aligned} &\quad + \left. \frac{1}{i\xi(u+i\xi)} + \frac{1}{(u+i\xi)^2} \right\} du \\ &= \frac{Y}{4\xi^2} \left[e^{-Yi\xi} \operatorname{erfc} \left(\frac{Y}{2\sqrt{T}} - i\sqrt{T}\xi \right) \left(\frac{1}{\xi} - 2i\xi + Y \right) \right. \\ &\quad + e^{Yi\xi} \operatorname{erfc} \left(\frac{Y}{2\sqrt{T}} + i\sqrt{T}\xi \right) \left(-\frac{1}{\xi} + 2i\xi + Y \right) \\ &\quad \left. - \frac{4\sqrt{T}}{\xi} e^{-\xi^2 - \frac{Y^2}{4T}} \right] \quad (A-9) \end{aligned}$$

$$\mathcal{L}^{-1}\{f_4(p)\} = \mathcal{L}^{-1} \left\{ \frac{e^{-i\xi Y}}{P^2 \sqrt{P+3^2} ((P+3^2 - \xi^2))} \right\}$$

With $P+\xi^2 = S$,

$$\mathcal{L}^{-1}\{f_4(p)\} = \frac{e^{-\xi^2 T - i\xi Y}}{2\pi C} \int_{R-i\infty}^{R+i\infty} \frac{e^{sT}}{(s^2 + (15+1\xi)^2)^2 (s^2 - \xi^2)^2} ds$$

After the contour integral,

$$\mathcal{L}^{-1}\{f_4(p)\} = \frac{1}{\pi} e^{-\frac{\xi^2}{3}} \int_{-\infty}^{\infty} \frac{e^{i\xi s}}{(s(s+\xi)^3)} ds$$

Let $u^2 = s$

$$\begin{aligned} \mathcal{L}^{-1}\{f_4(p)\} &= \frac{e^{-\frac{\xi^2}{3}}}{16\pi\xi^2} \int_0^\infty e^{-u^2} \left\{ \frac{i}{(u+i\xi)^3} - \frac{i}{(u-i\xi)^3} \right. \\ &\quad \left. - \frac{3i}{13^2(4-u^2)} - \frac{2i}{(u+i/\xi)^3} - \frac{-3}{13^2(4+u^2)} + \frac{2i}{13^2(4+i/\xi)^3} \right\} du \\ &= \frac{1}{2\xi^2} \left\{ (4T - 4T\xi^2 - \frac{3}{\xi^2}) \operatorname{erf}(T\xi/13) \right. \\ &\quad \left. - \frac{2T}{\pi} e^{-\frac{\xi^2}{3}} (2T/\xi - \frac{3}{\xi^2}) \right\} \quad (A-10) \end{aligned}$$

Equations (A-8), (A-9) and (A-10) are substituted to equation (A-7) and equation (33) is derived.

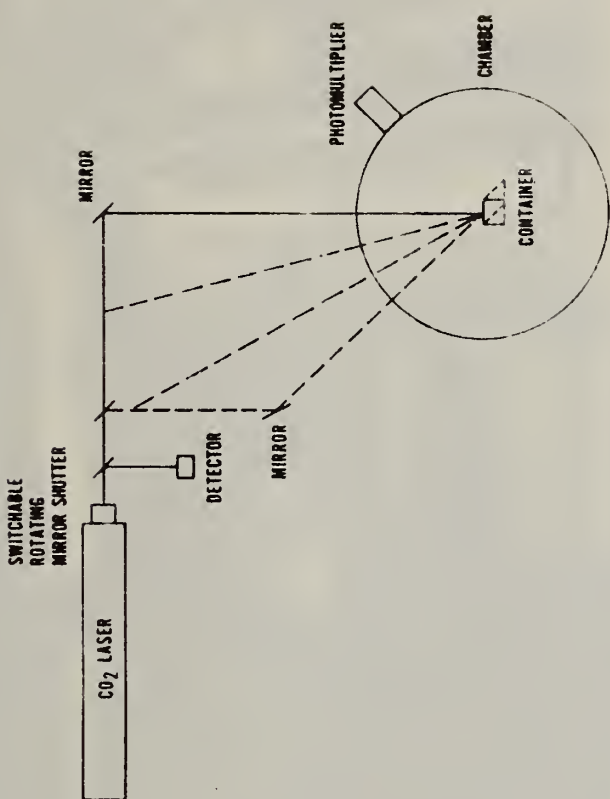


Fig. 1

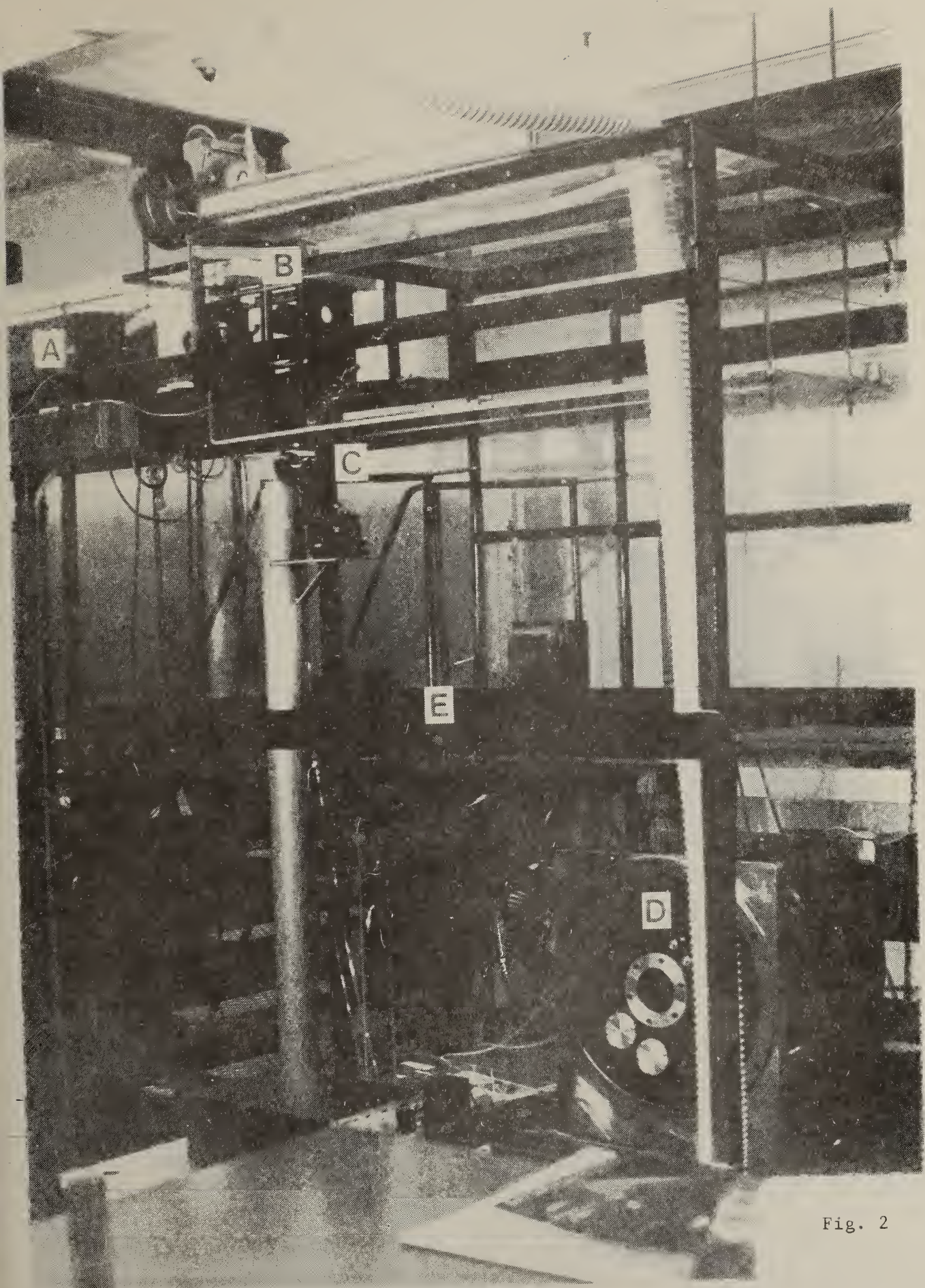
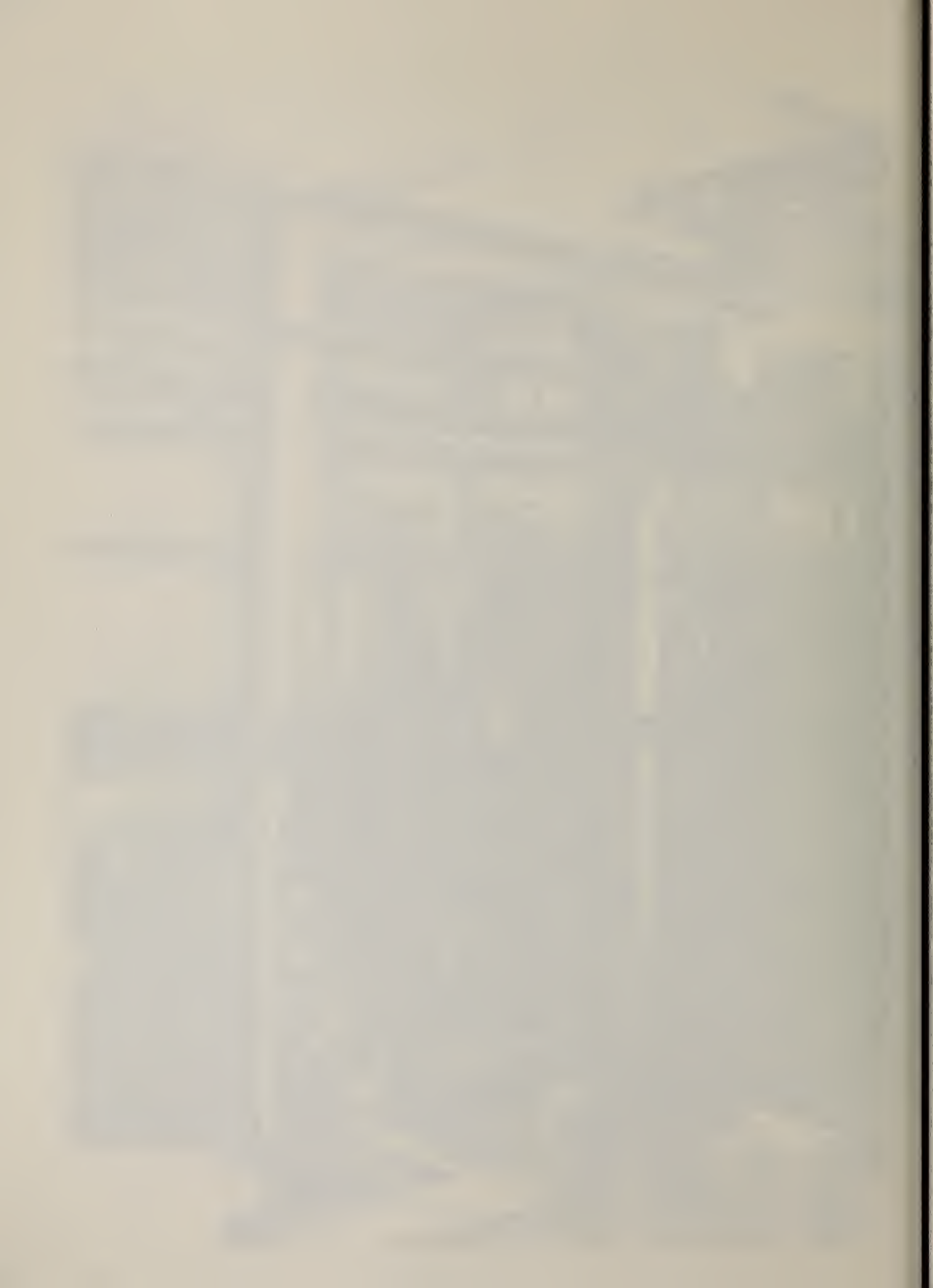


Fig. 2



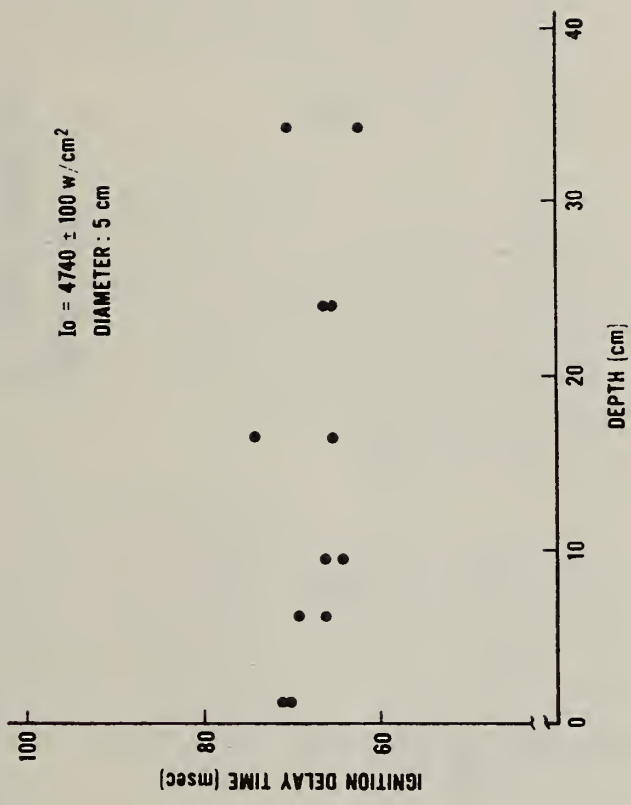


Fig. 3



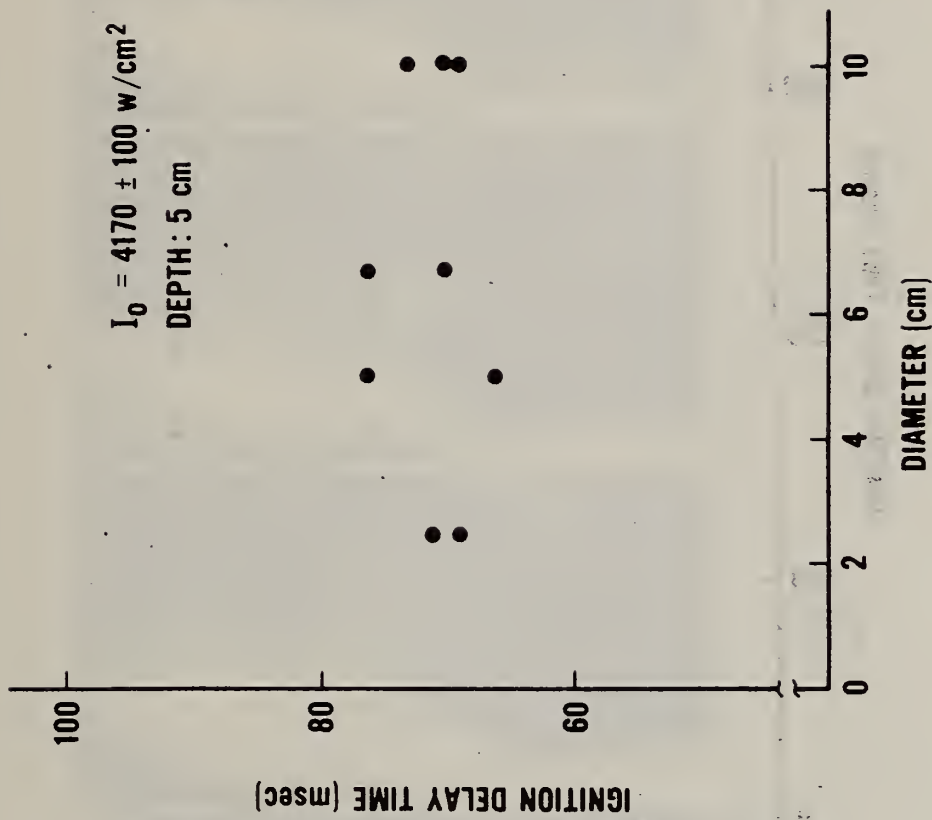


Fig. 4A

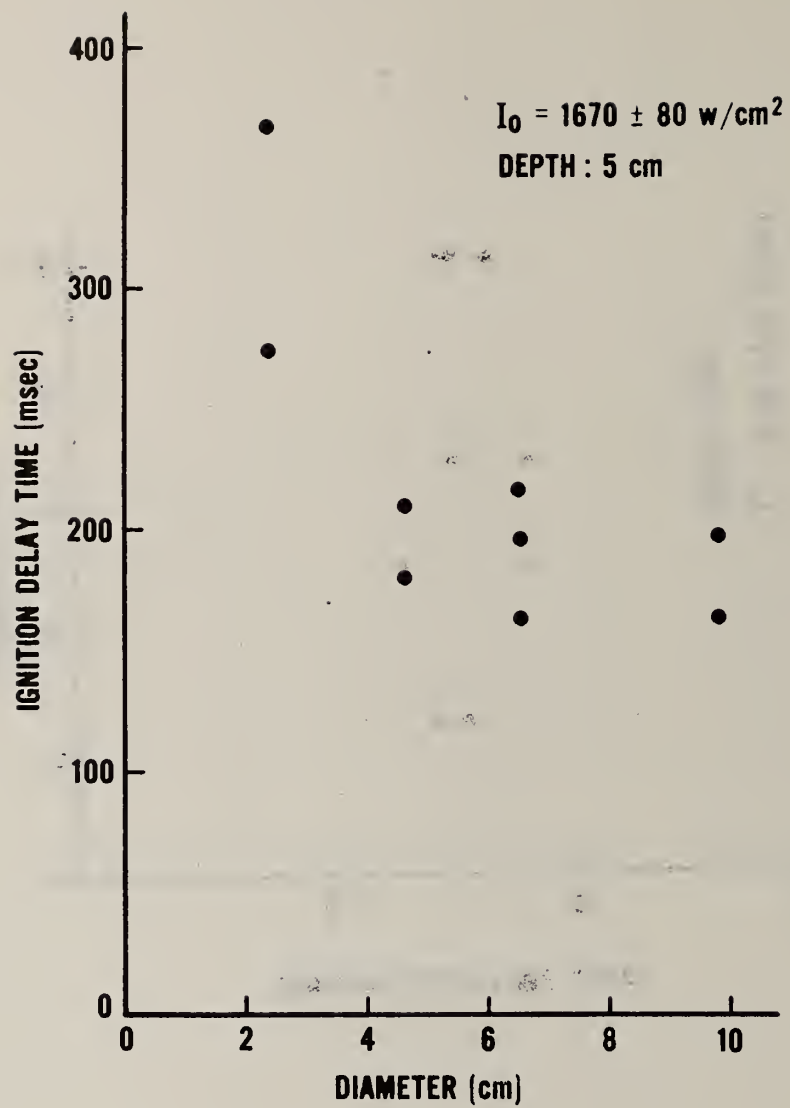
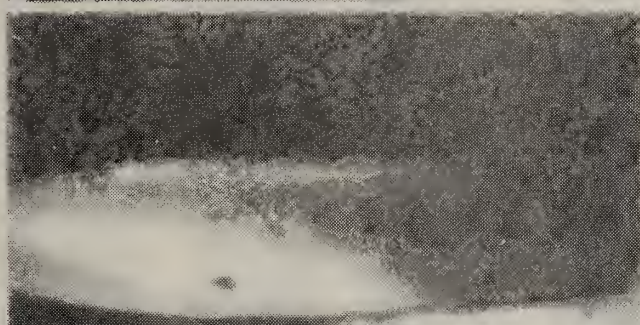


Fig. 4B



(a)



(b)



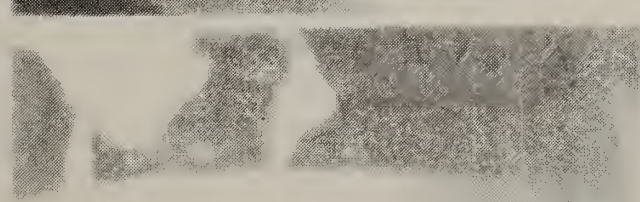
(c)



(d)



(e)



(f)

Fig. 5

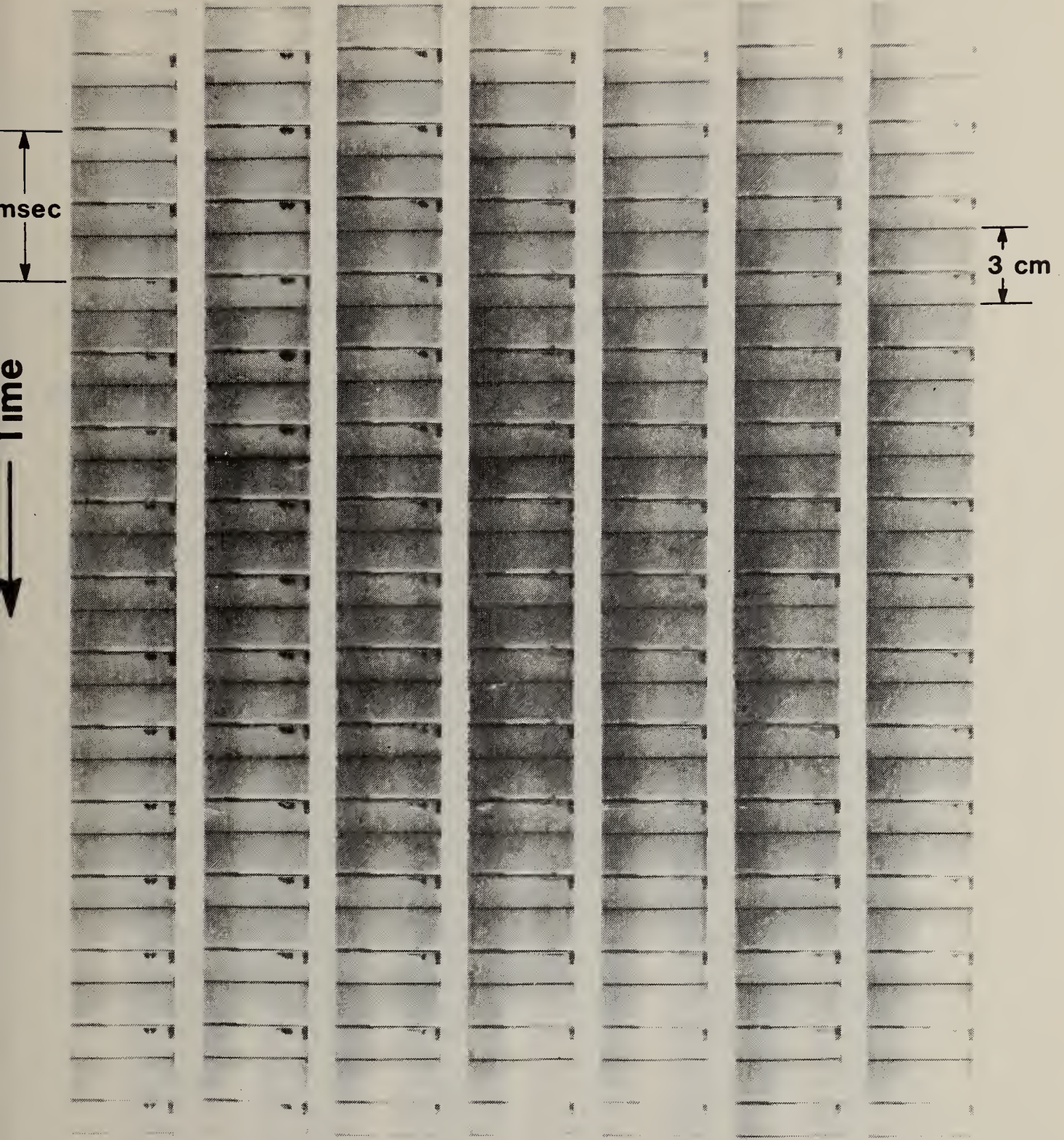
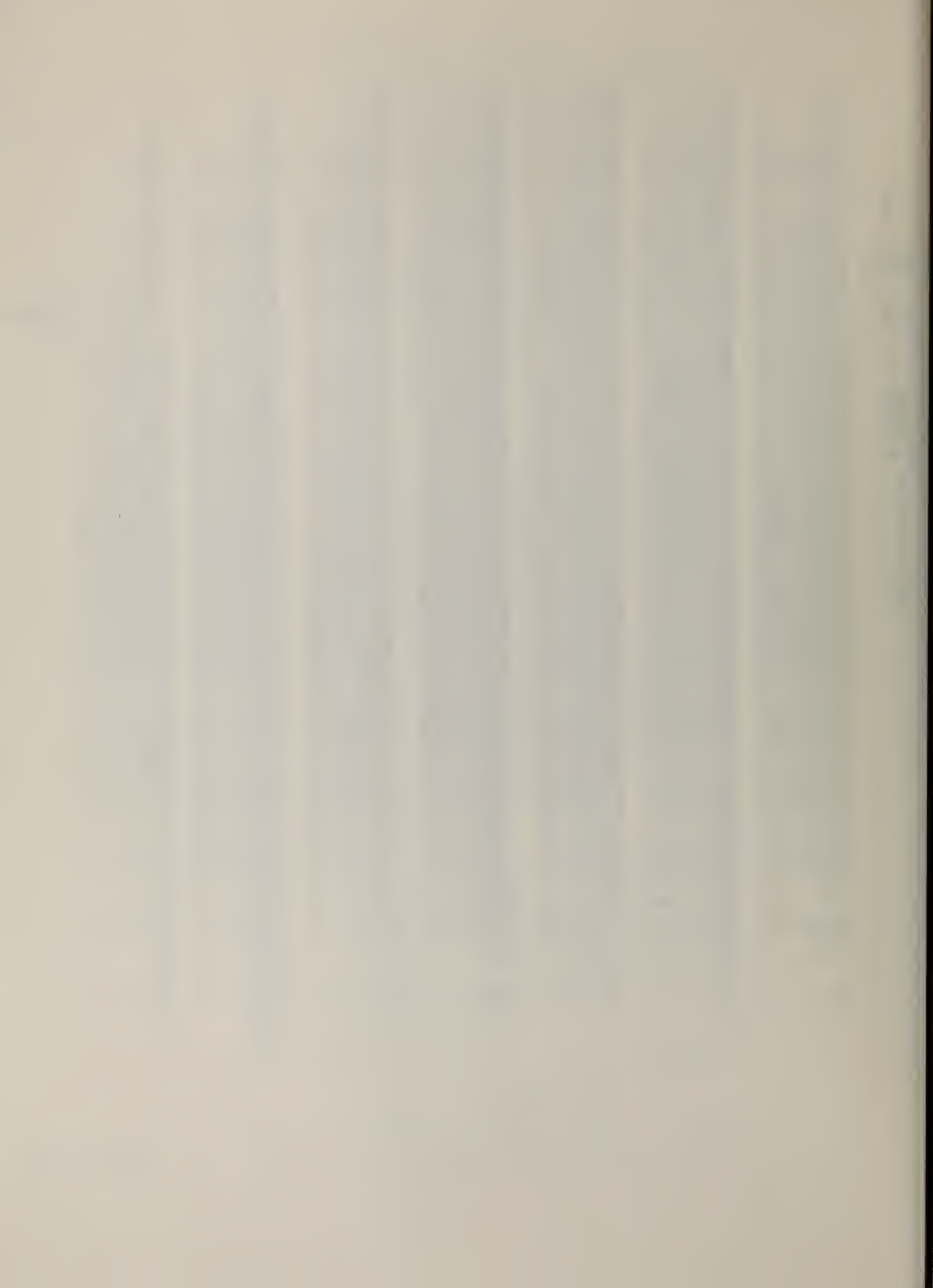


Fig. 6-Pt. 1



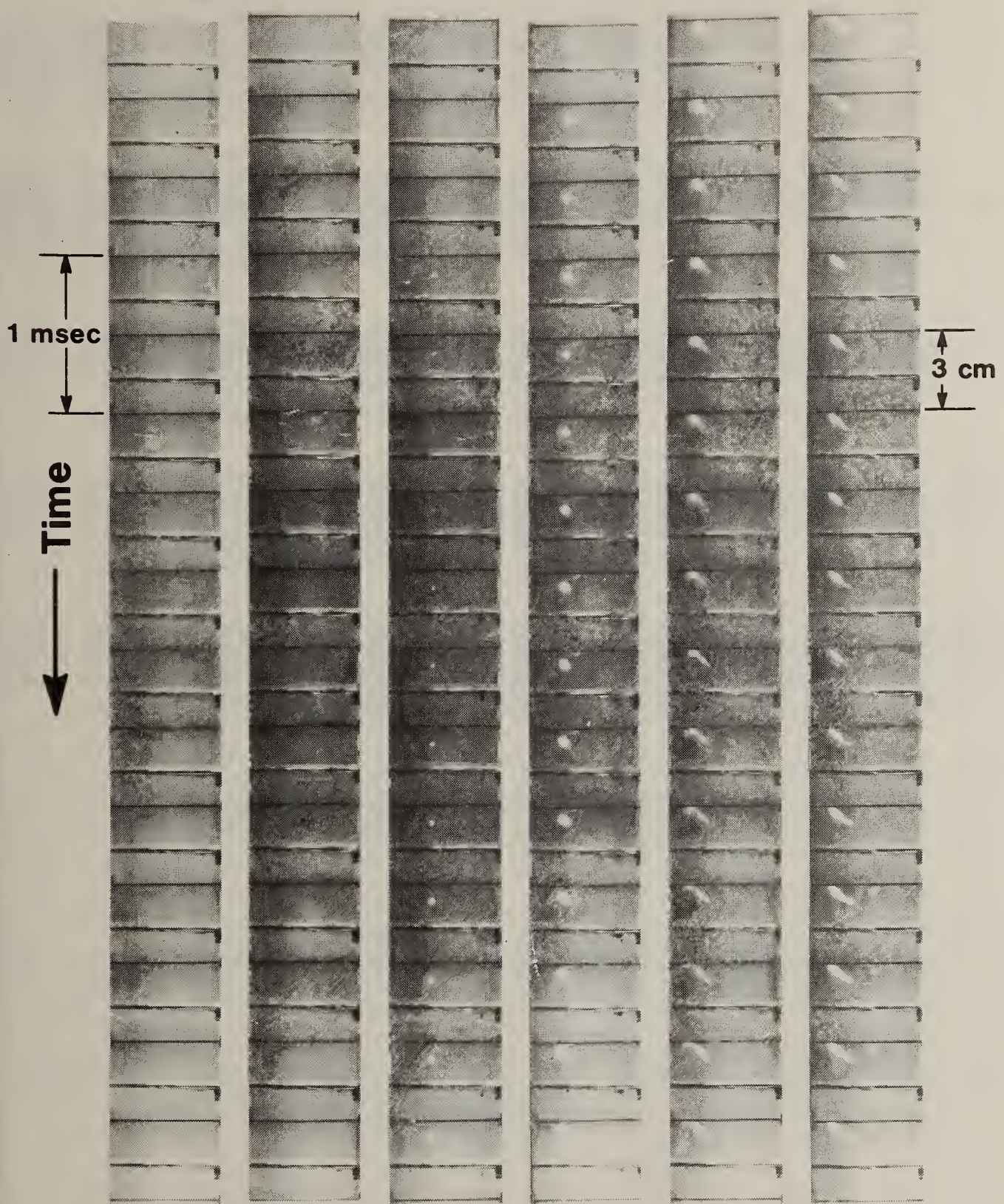


Fig. 6-Pt. 2



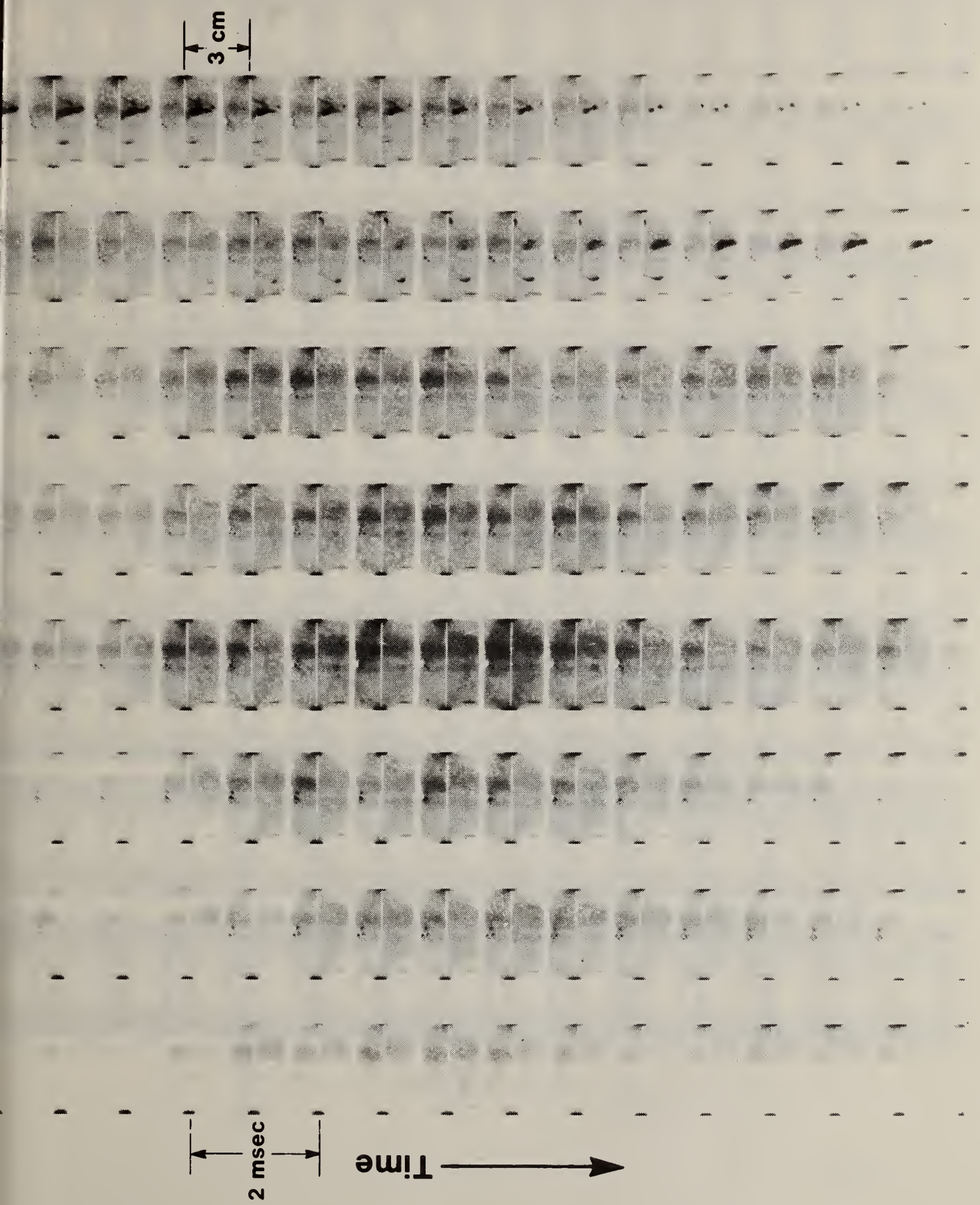
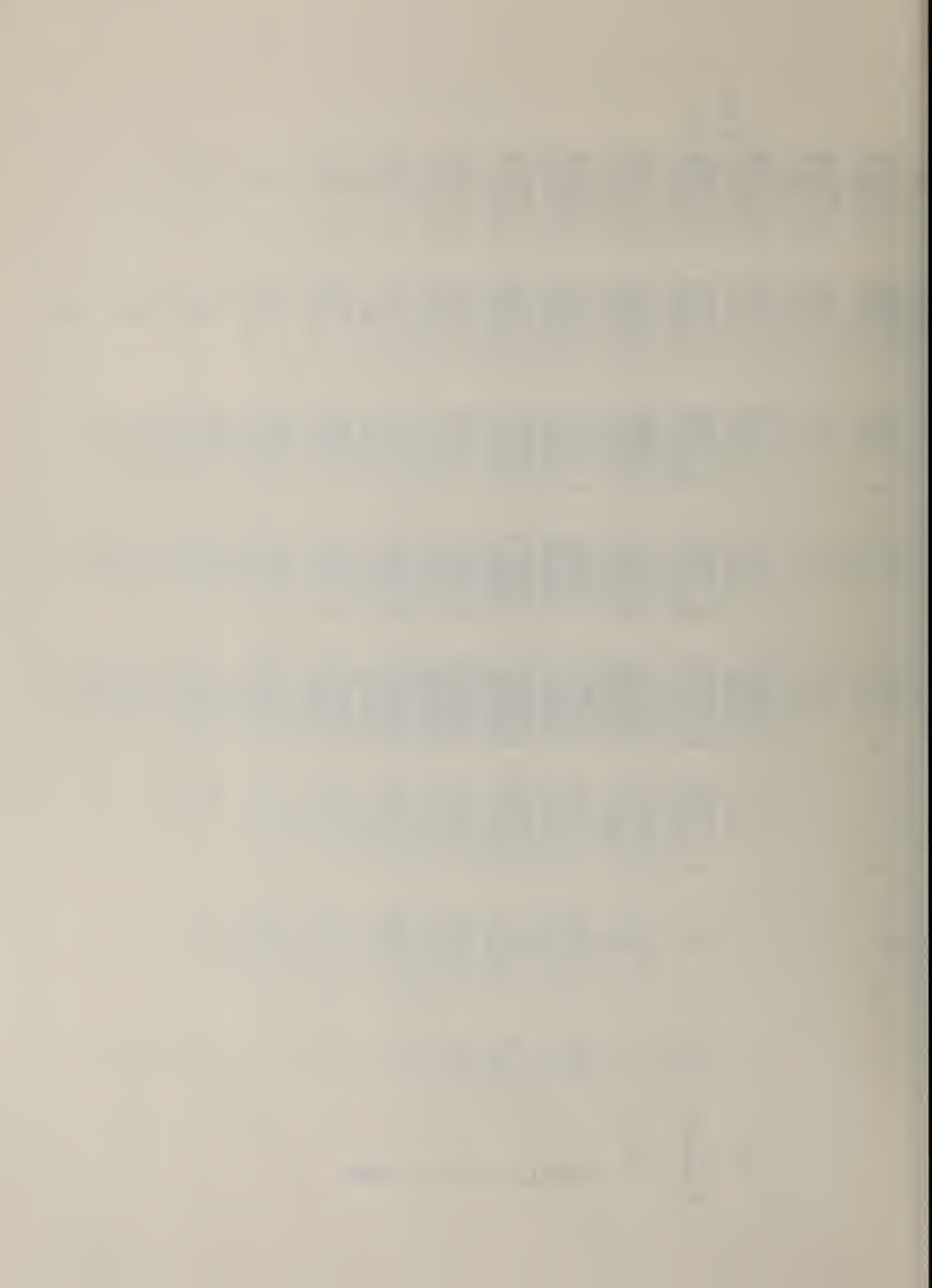


Fig. 7



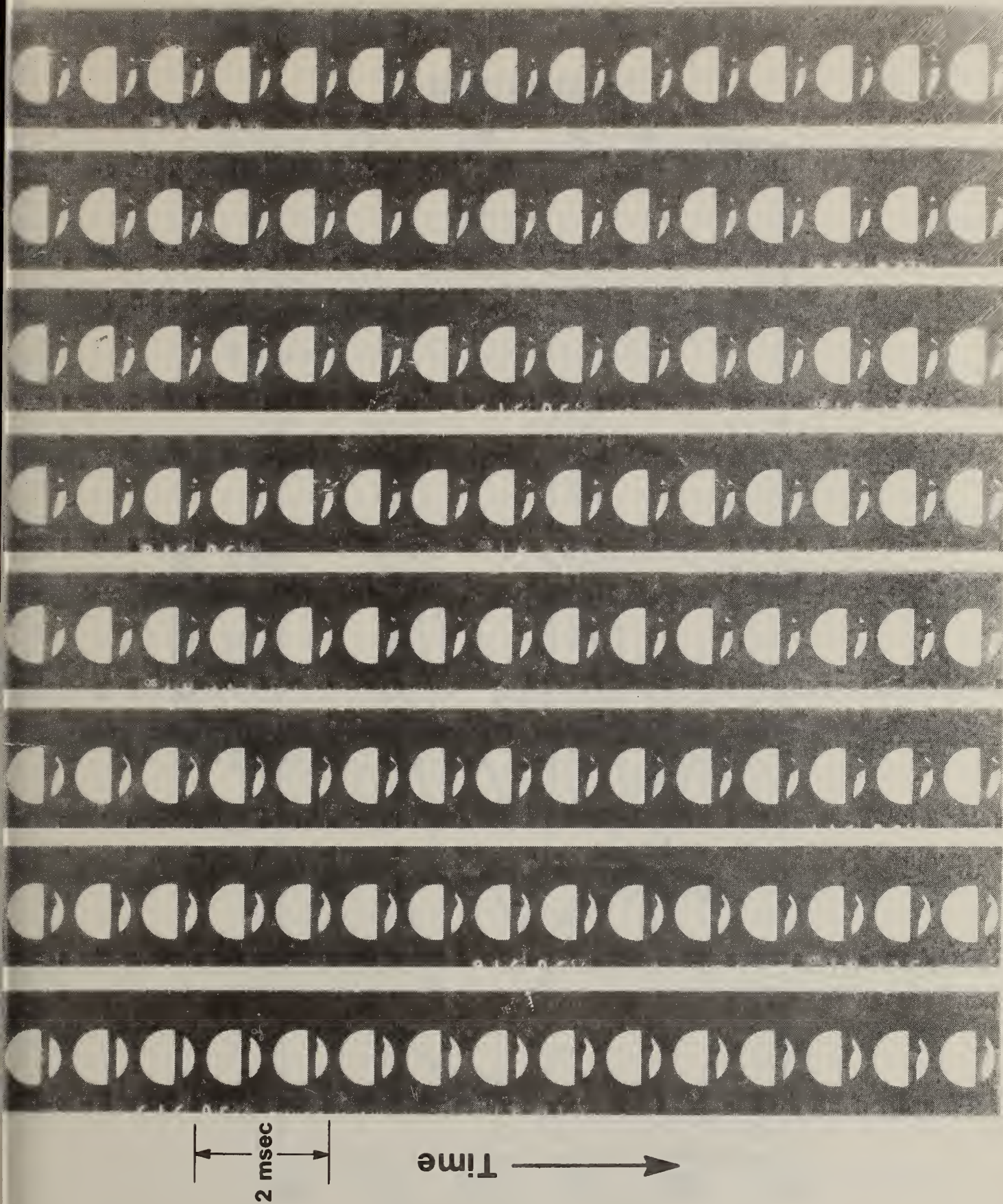
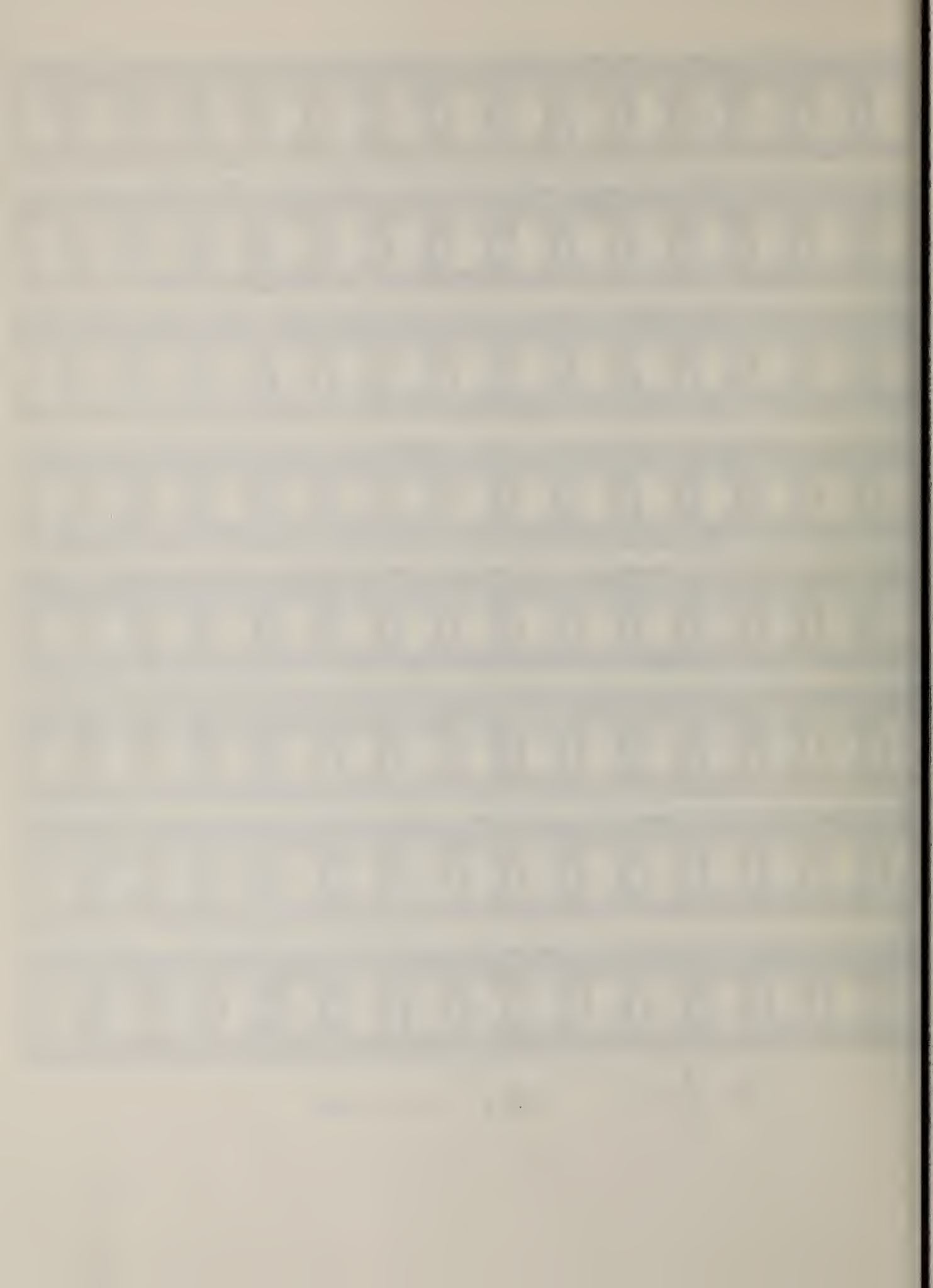


Fig. 8



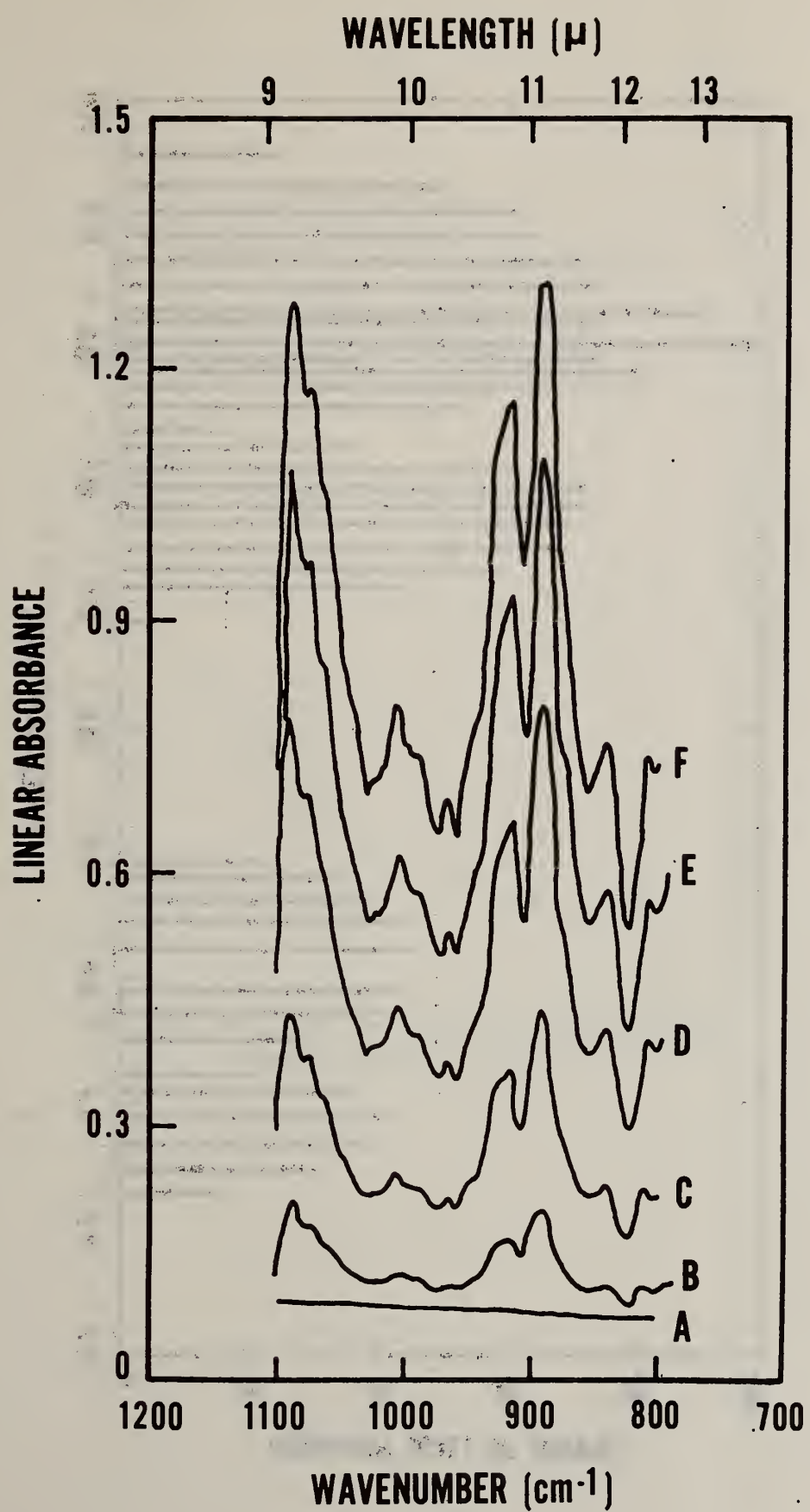


Fig. 9

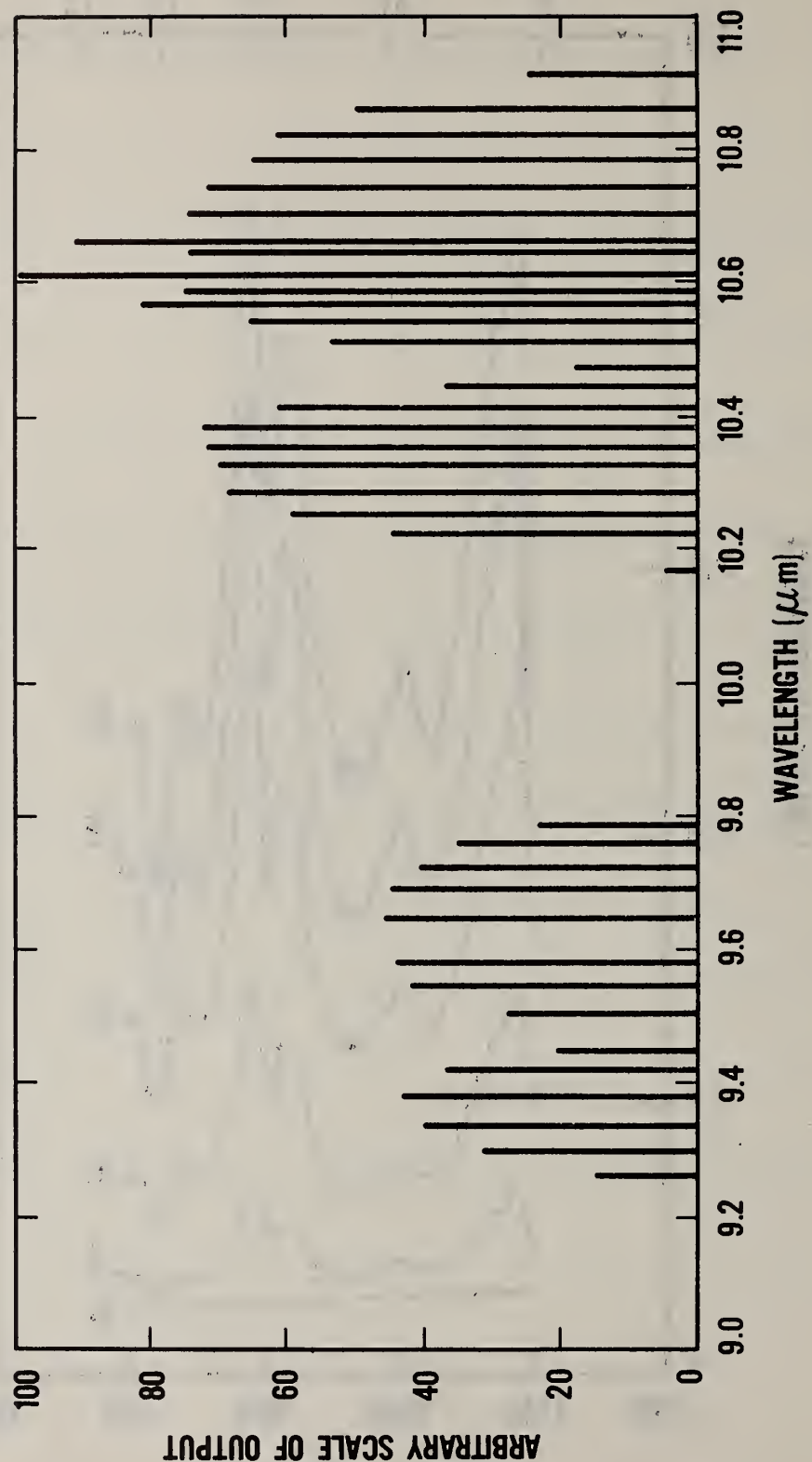


Fig. 10

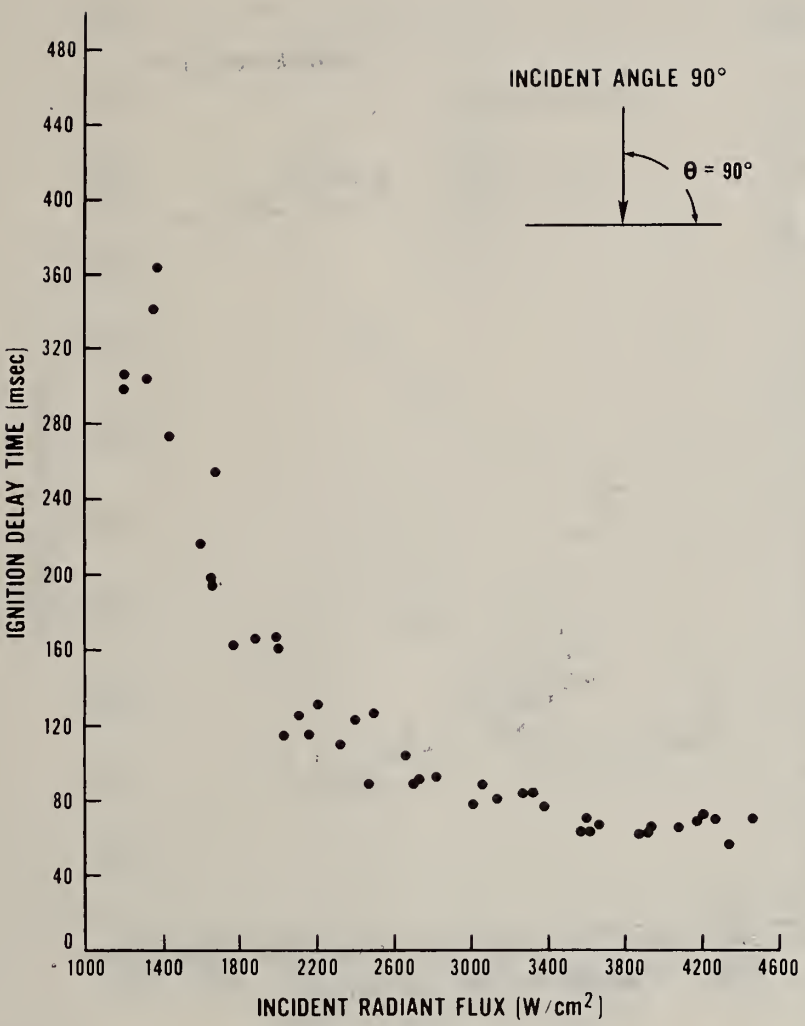


Fig. 11A

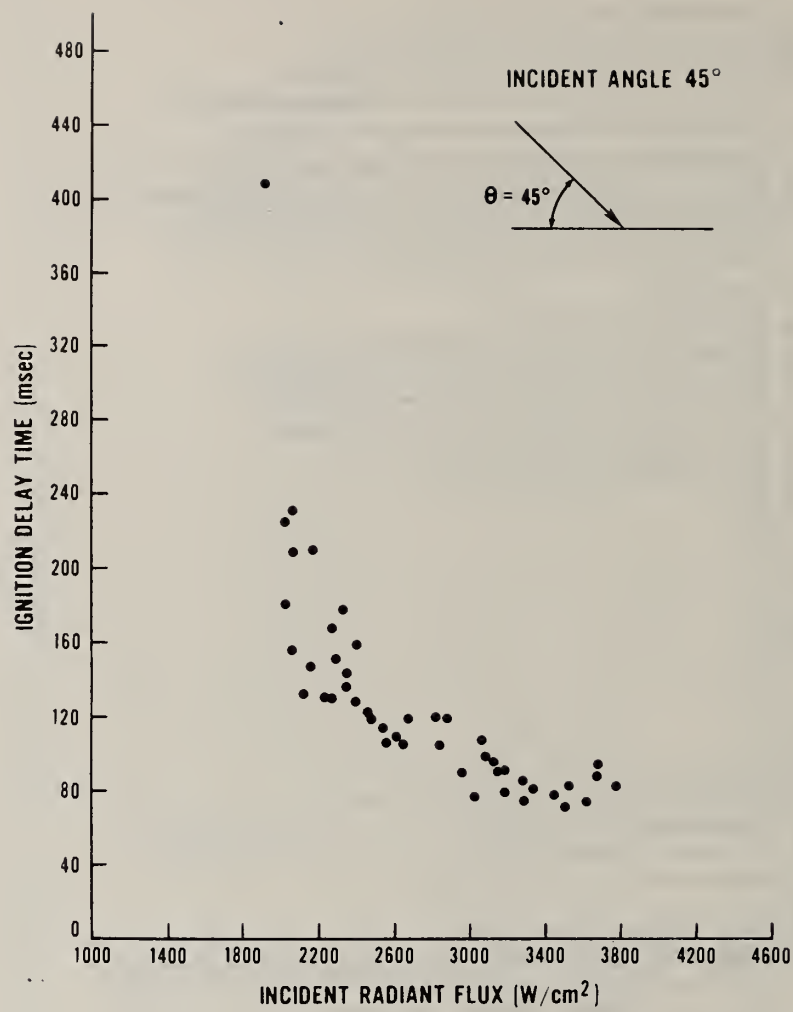


Fig. 11B

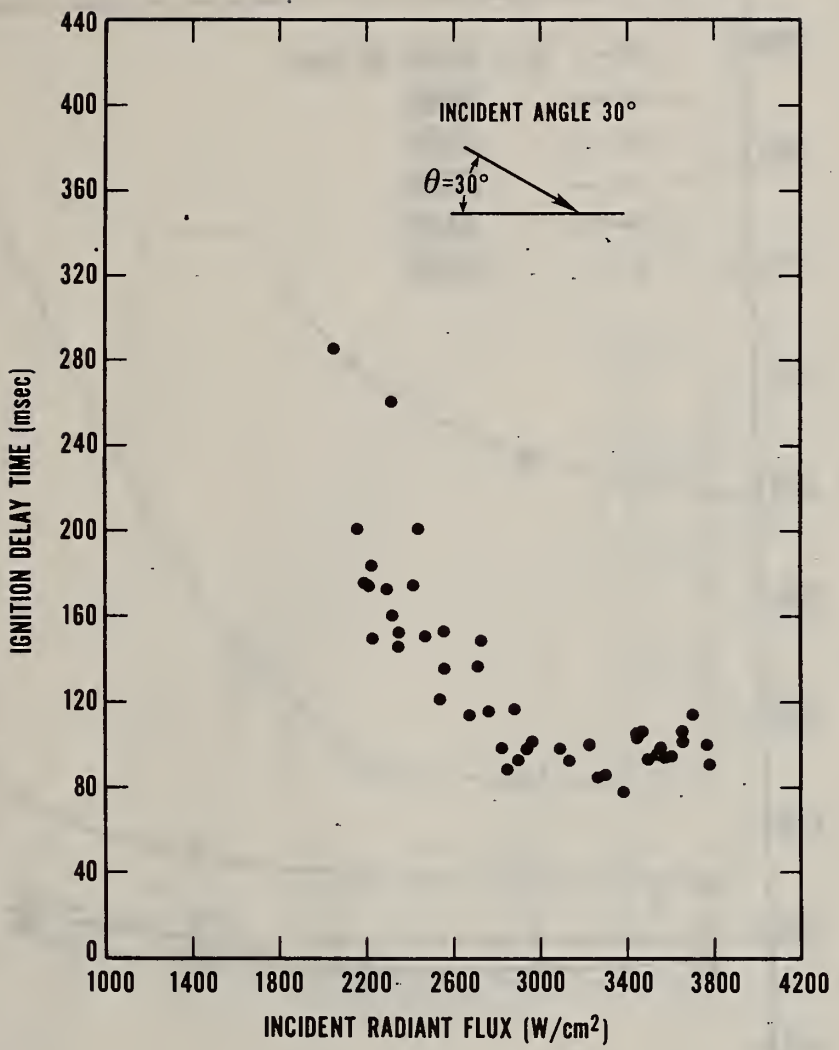


Fig. 11C

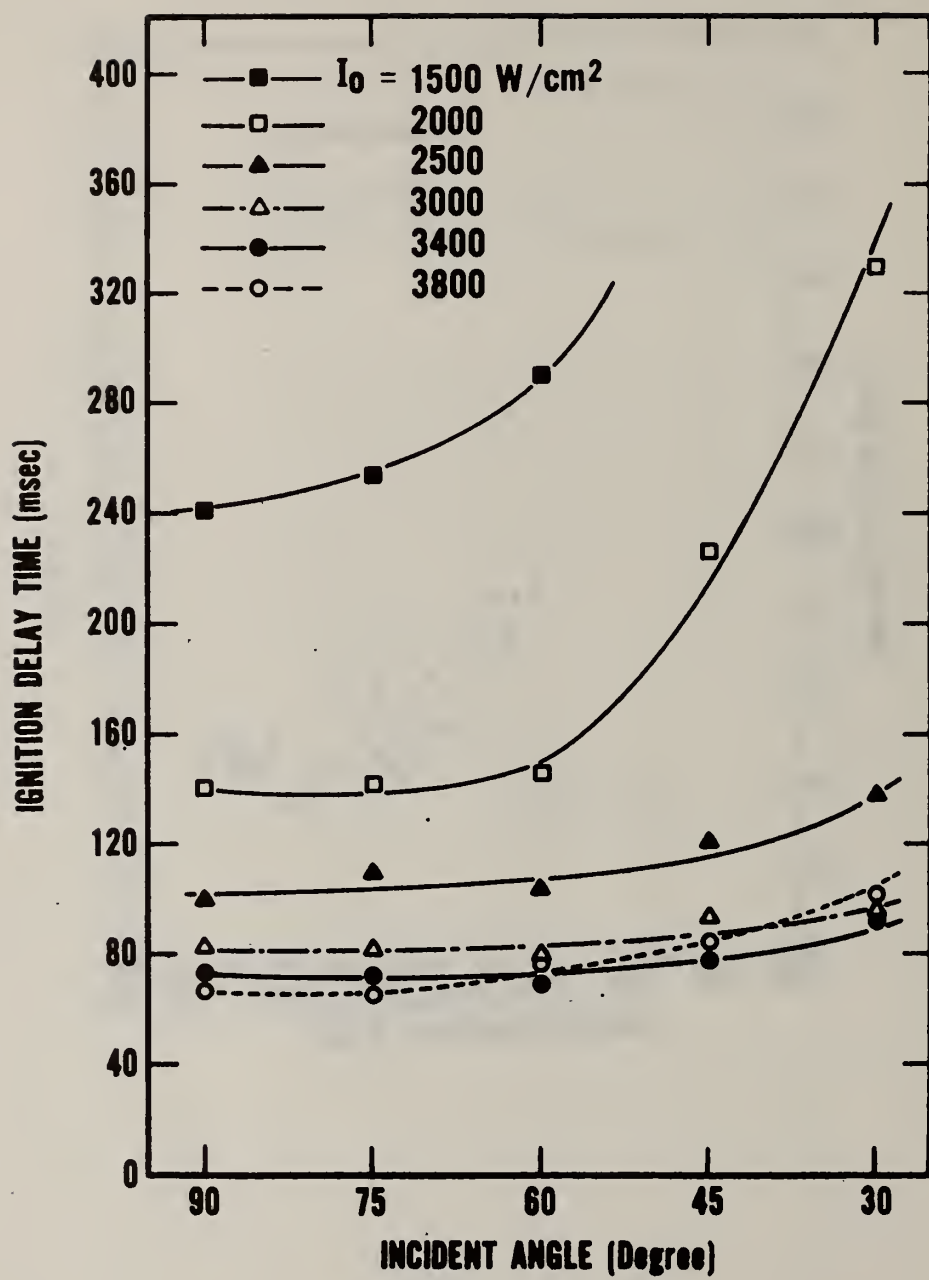


Fig. 12

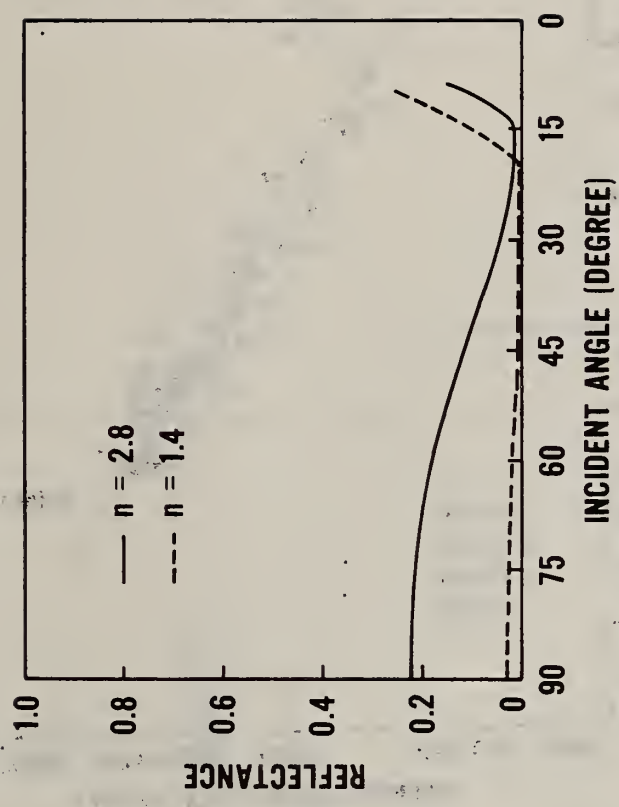


Fig. 13

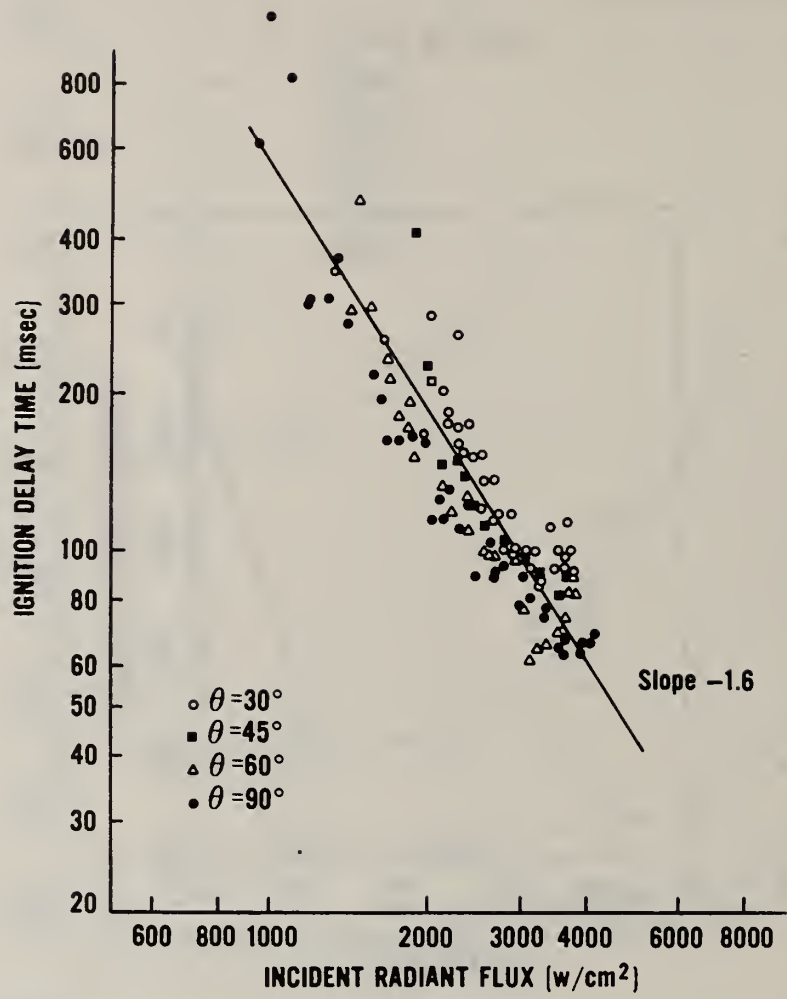


Fig. 14

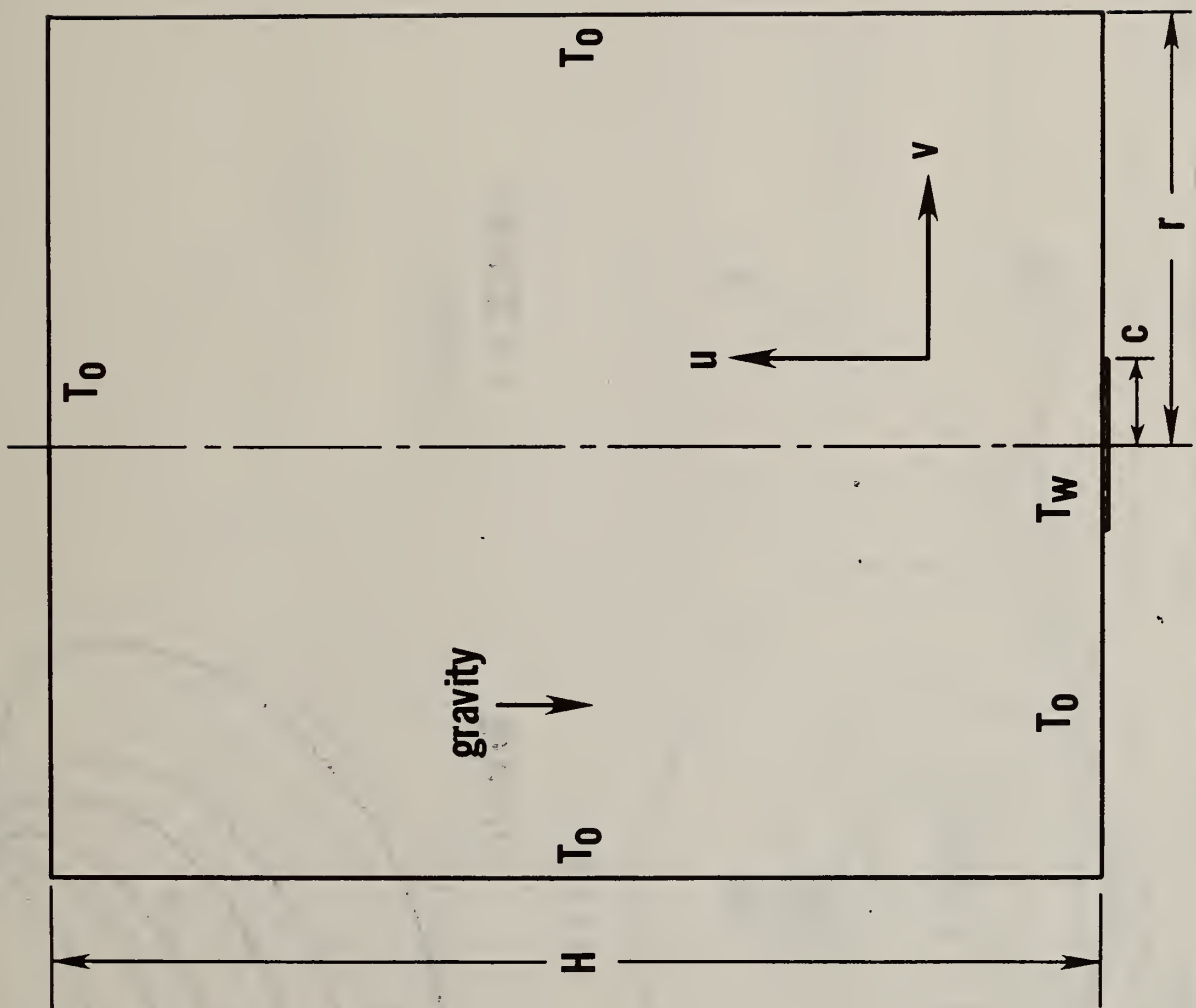


Fig. 15

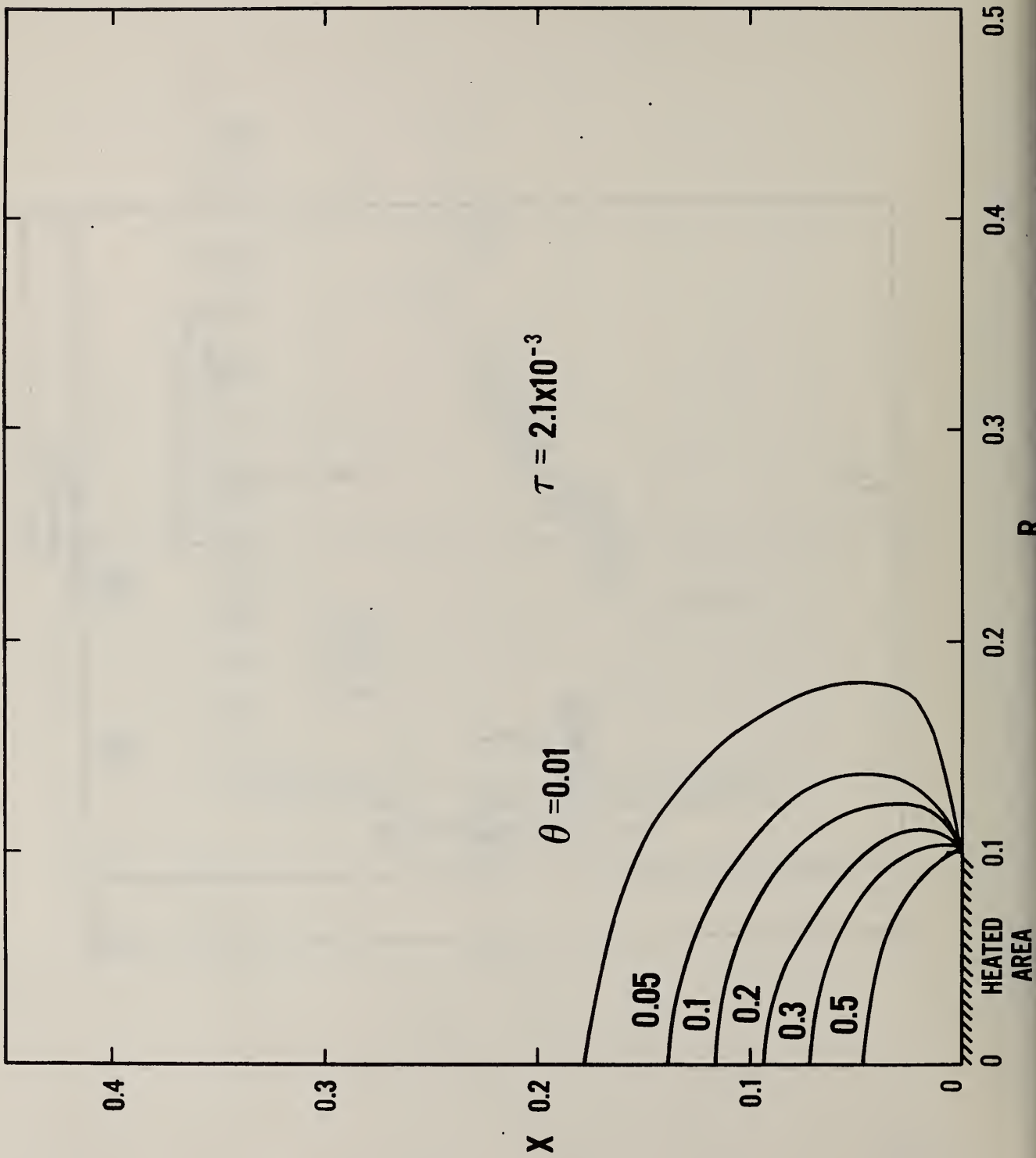


Fig. 16A

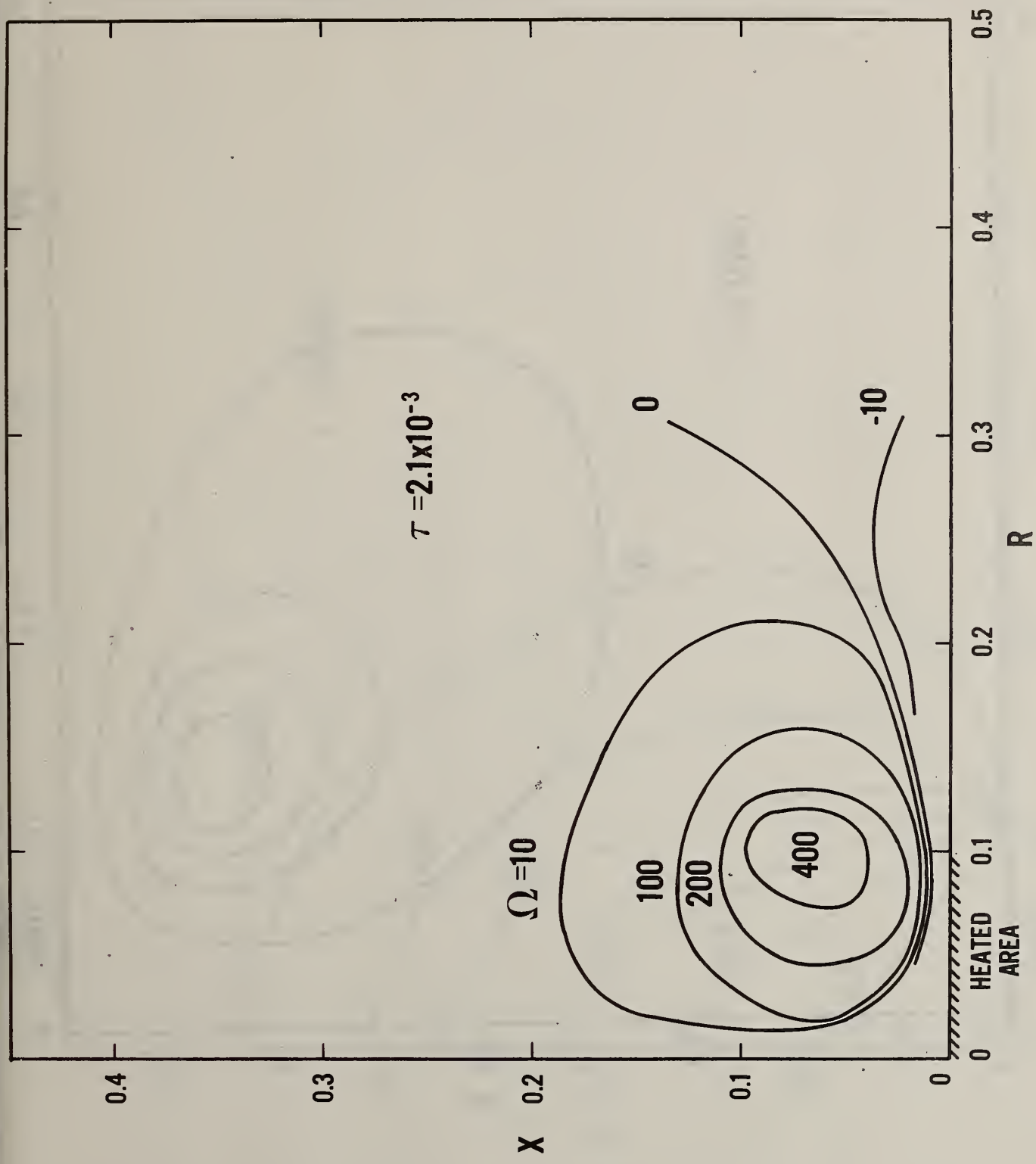


Fig. 16B

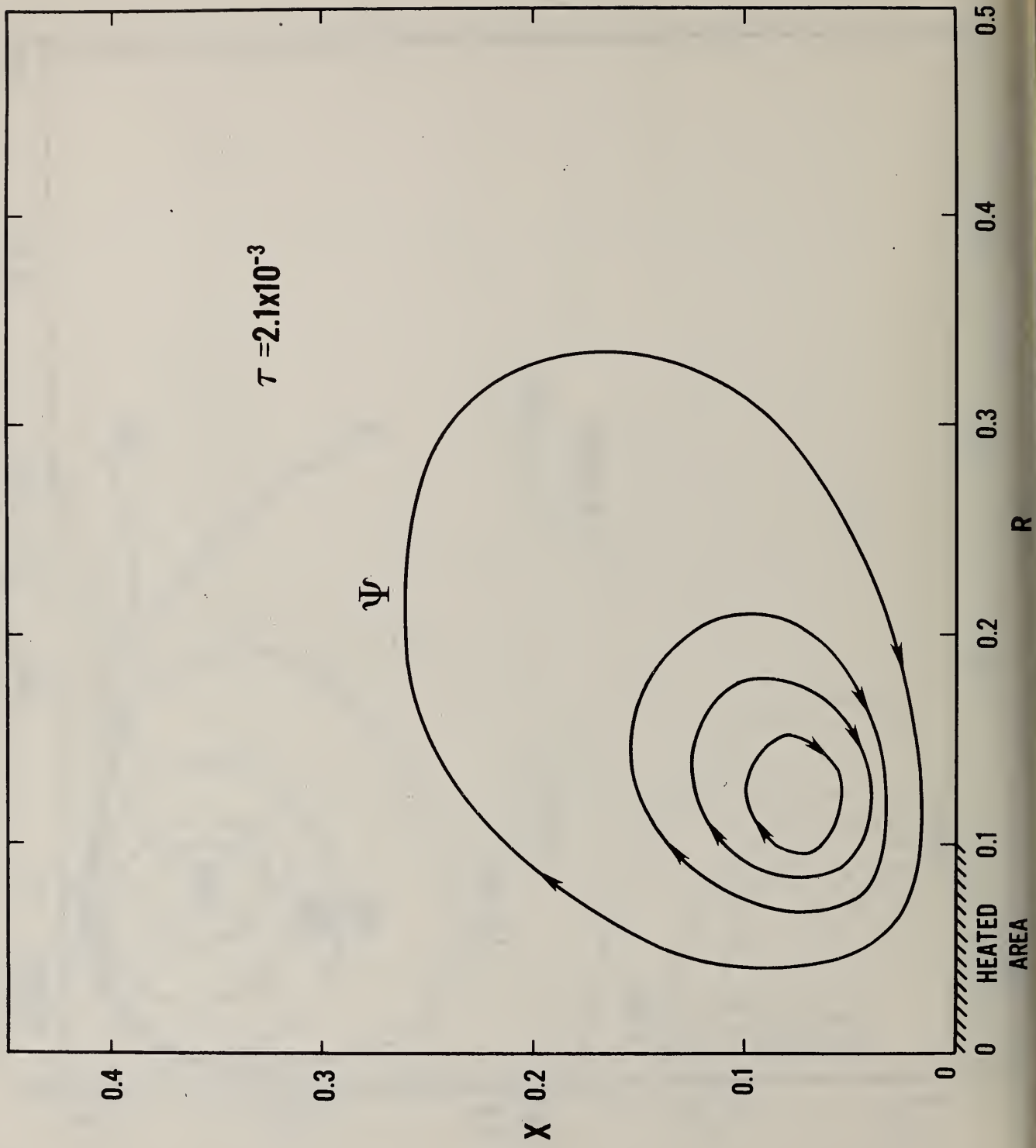


Fig. 16C

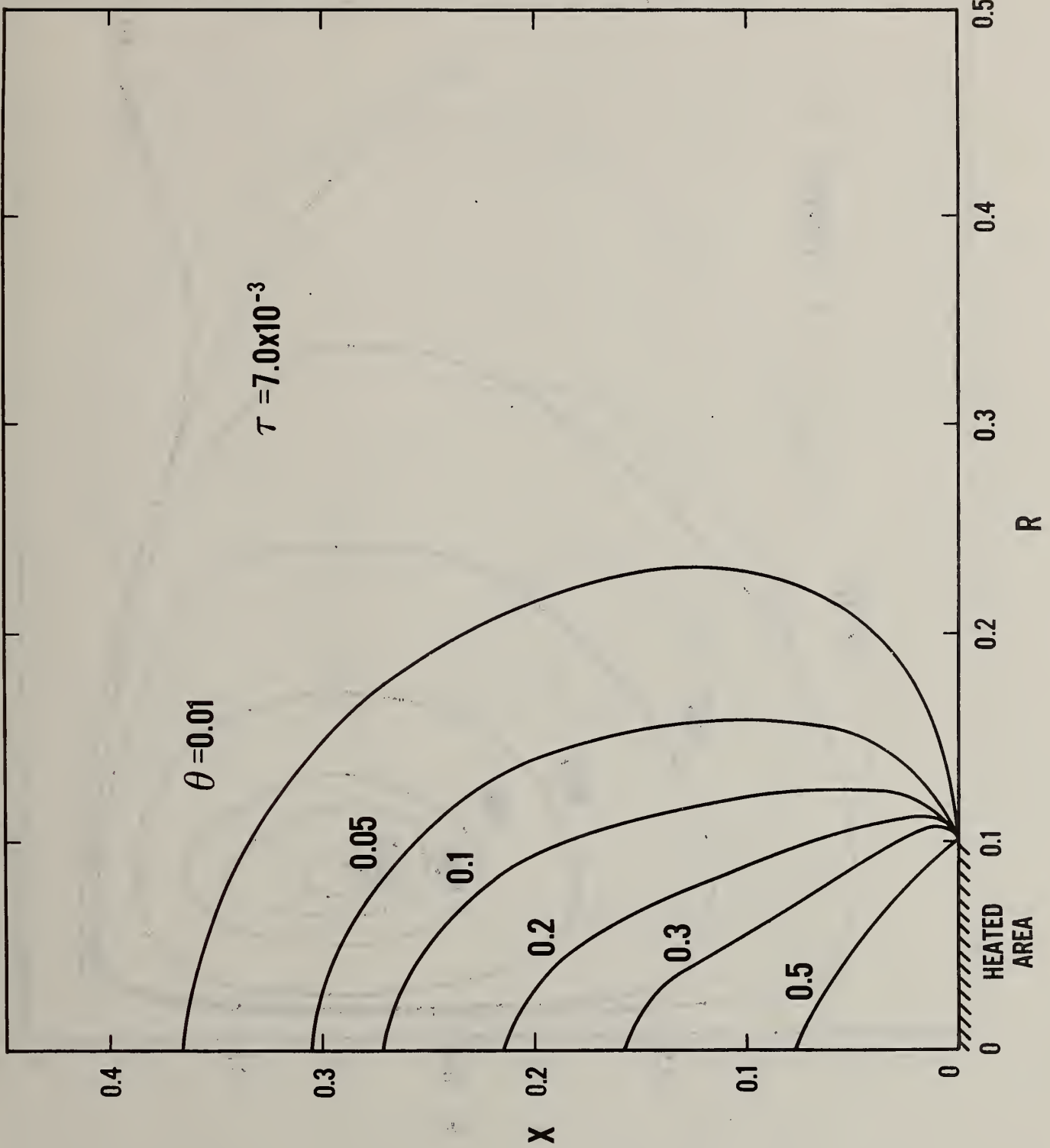


Fig. 17A

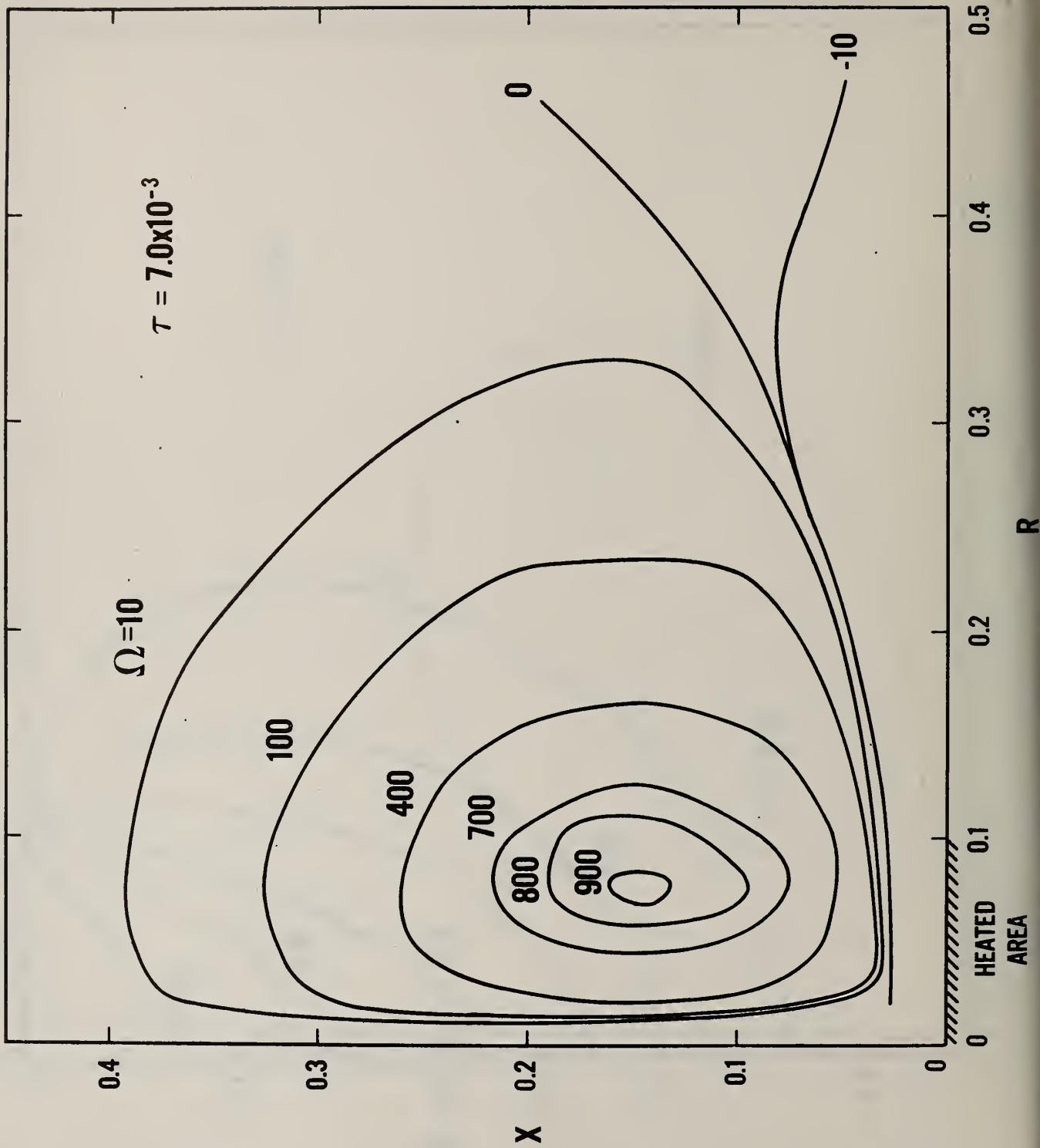


Fig. 17B

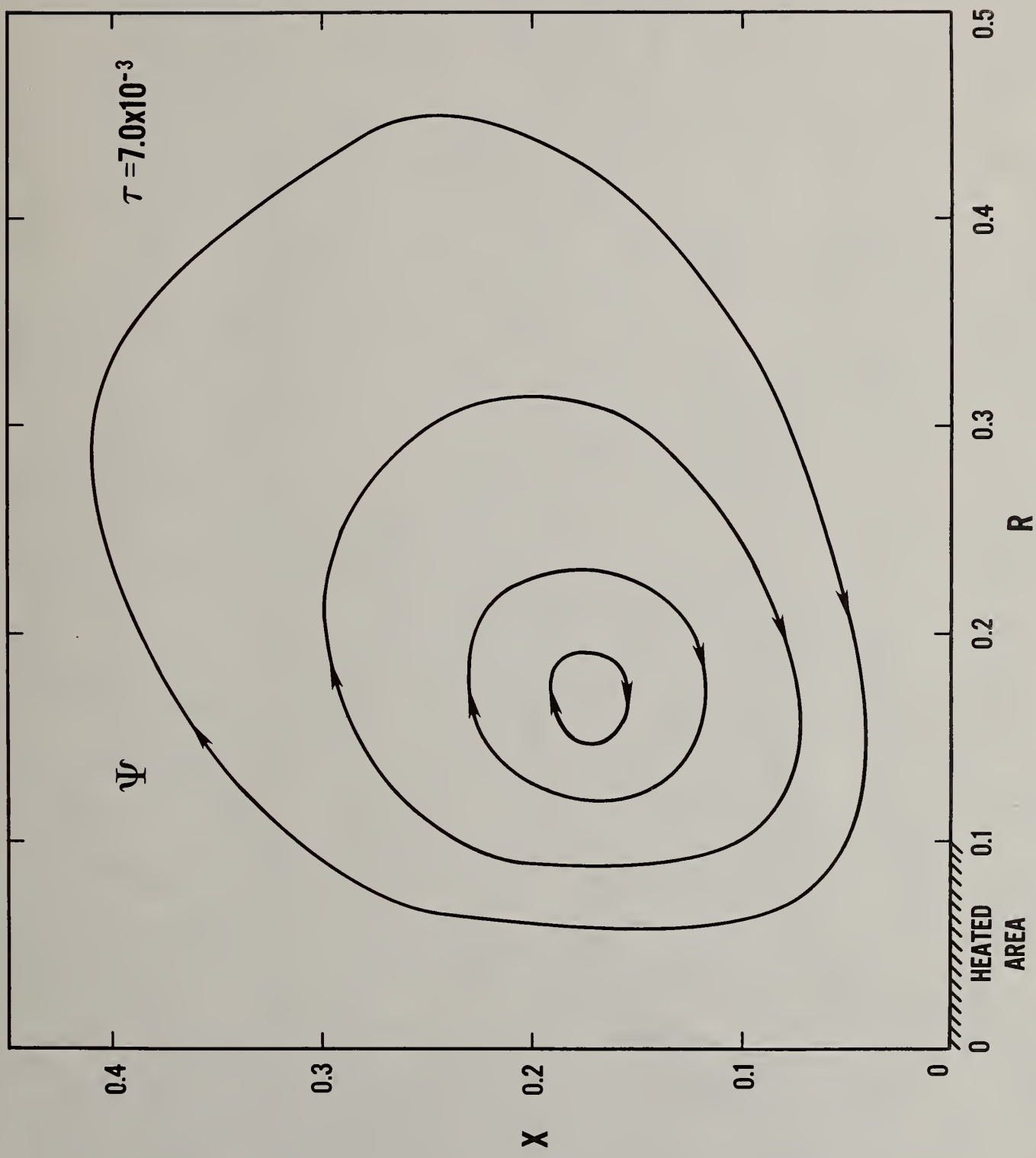


Fig. 17c

